Wang, W., Shao, H., **Nagel, T.**, **Kolditz, O.** (2021):
Analysis of coupled thermal-hydro-mechanical processes during small scale in situ heater experiment in Callovo-Oxfordian clay rock introducing a failure-index permeability model
Int. J. Rock Mech. Min. Sci. **142** , art. 104683

http://dx.doi.org/10.1016/j.ijrmms.2021.104683

Analysis of coupled thermal-hydro-mechanical processes during small scale in situ heater experiment in Callovo-Oxfordian clay rock introducing a failure-index permeability model

Wenqing Wang[a,*], Hua Shao[b], Thomas Nagel[d,a], Olaf Kolditz[a,c]

[a] *Helmholtz Center for Environmental Research - UFZ, Leipzig, Germany*

[b] *Federal Institute for Geosciences and Natural Resources - BGR, Hanover, Germany*

[c] *Technische Universität Dresden, Germany*

[d] *Technische Universität Bergakademie Freiberg, Germany*

Abstract

To better understand the coupled thermo-hydro-mechanical processes in Callovo-Oxfordian (COx) claystone formations induced by heat emitting high-level radioactive waste, different scales of in-situ heater experiments have been conducted by ANDRA in the Meuse/Haute-Marne Underground Research Laboratory (M/HM URL) at Bure in France. In order to prove the predictability of numerical codes for a site-scale repository, two experiments, a small-scale (TED) and a full-scale experiment (ALC), have been intensively investigated by different teams within the international project DECOVALEX 2019. In this study, we present the numerical results obtained further developing and using the finite element OpenGeoSys (OGS) simulator with two novel approaches. (1) A failure index-dependent permeability model is introduced into the THM formulation to consider the effect of the permeability changes in the excavation-damaged zone (EDZ) on the pore pressure development during the excavation and subsequent heating phases, respectively. (2) A more general equation of state formulation for water according to the International Association for the Properties of Water and Steam (IAWPS) taking account of water and vapour behaviour is implemented to simulate the pore pressure increase induced by high temperature during heating. The complete model comparison study is presented in the Task E synthesis paper [49].

Keywords: DECOVALEX, thermo-hydro-mechanical (THM) processes, heater experiment in clay rock, Meuse/Haute-Marne Underground Research Laboratory, failure-dependent permeability model, OpenGeoSys

---

* Corresponding author
Tel: +49-341-235-1883
Email address: wenqing.wang@ufz.de (Wenqing Wang)

1. Introduction

Process and safety analyses are an integral part of the long-term safety assessment for nuclear waste disposal options. For this purpose, a comprehensive understanding of the long-term multi-physical (thermo-hydro-mechanical) and chemical processes within the repositories is essential and has to be based on both experimental and modelling works. The study of thermo-hydro-mechanical (THM) processes in clay formations and clay materials is a subject of intensive research regarding the nuclear waste management [53]. Several clay formations are of interest for national repository concepts depending on their characteristics and abundance in various countries, i.e. Boom clay in Belgium [37, 36], Opalinus clay (OPA) in Switzerland [8, 39] and Callovo-Oxfordian (COx) in France [44, 43]. Bentonite as a potential sealing material within clay host rocks is under intensive investigation as well [25]. Similarities in the material behaviour of clay-rich rocks and bentonite materials are of certain interest for developing related constitutive models [56]. Significant research on Opalinus clay has been conducted in the Underground Research Laboratory Mt. Terri [7]. Several experiments there have been included as tasks into previous DECOVALEX phases. Garitte et al. [22, 23] presented the numerical modelling of the coupled THM processes in a bedded argillaceous formation (Opalinus Clay) based on the in-situ heater experiments (HE-D and HE-E), respectively.

In the 1990s, the French National Radioactive Waste Management Agency (ANDRA) began the investigation of Callovo-Oxfordian claystone (COx) as a potential host rock for radioactive waste disposal in the eastern part of the Paris Basin. The suitability of COx was identified based on properties such as a very low intrinsic permeability [21, 29] and excellent self-sealing capabilities [41]. The Meuse/Haute-Marne Underground Research Laboratory (M/HM URL) was consequently established by ANDRA in the year 2000 for a detailed investigation of COx under in-situ conditions. Since then, many experiments and studies have been conducted at M/HM URL by ANDRA and its associated researchers in order to demonstrate the feasibility of constructing and operating a radioactive waste disposal facility in the COx claystone [3, 18, 27, 4].

Among these studies, an extensive experimental program has been conducted since 2005 which aims at investigating the thermo-hydro-mechanical (THM) response of the COx to thermal loading by potential heat emitting radioactive waste. The program consists of two combined in-situ experiments operated at different scales: 1) a small-scale experiment for heating boreholes (the so-called TED experiment) and 2) a full-scale experiment (the so-called ALC experiment), cf. [4]. Both experiments were intensively investigated as part of the international DECOVALEX Project in its seventh phases from 2016 to 2019 to analyse related scale effects and to prove the predictability of the developed numerical model for a realistic disposal scenario. The experimental studies are mainly aimed at quantifying material properties [11, 24, 15] which will be then used for numerical modelling of the long-term evolution of the THM variables in the nuclear waste disposal repository. A selection of related THM material properties of COx at the M/HM URL site was summarised by Armand et al. [4] and provides the basis for the present study. Some studies already exist for the characterisation of COx material properties under HM conditions. Pardoen et al. [44] simulated fracturing around a drift in COx to estimate the damage zone by taking into account strain localisation. Guayacan-Carrillo et al. [26] studied the pore pressure evolution during the drift excavation by considering the effects of mechanical anisotropy of COx and hydro-mechanical coupling. With a 2D example, Guayacan-Carrillo et al. [26] also presented results of the failure analysis and the associated tendency of permeability increase in the EDZ. To characterise migration of hydrogen produced from the corrosion of steel containers through the initially water-saturated COx, Mahjoub et al. [38] simulated two laboratory tests of gas injection in the water-saturated COx under HM coupling.

For numerical analysis such as the ones reviewed above, the first essential requirement is to define the initial boundary value problem (IBVP) which mainly includes three steps: (1) establishing the governing balance equations for the determination of the primary field variables; (2) selecting or developing **constitutive models** that can represent the physical properties of the material as closely as required and that, mathematically speaking, are required to close the system of balance equations; and (3) determining reasonable initial and boundary conditions. In practical analyses, the last step is far from trivial but not a focus of the current paper. Finding suitable constitutive models (2) consistent with the described IBVP (1) is crucial for performing meaningful analyses and still requires significant effort both in terms of experimental and of theoretical work. One example of such a constitutive relationship is Fourier's law establishing a linear relationship between the temperature gradient and the conductive heat flux by introducing the thermal conductivity tensor. Other examples include the equations of state for fluids described later.

As will become evident from the presented results, the increase of the permeability in the EDZ by several orders of magnitude [9, 20, 11, 18] associated with brittle failure of the COx [2] needs to be captured by the constitutive model in order to predict pore pressure evolution. Early studies on permeability changes in porous media established their connection to porosity changes, which resulted, among others, in the renowned Kozeny-Carman equation [34, 10]. The Kozeny-Carman equation was often modified to fit different permeability properties in different porous media, e.g. the one by [16] for non-granular systems such as fiber mats and vesicular rocks. For COx, Chavant and Fernandes [13] proposed an exponential function of porosity for permeability determination, which was applied to the simulation of hydraulic permeability evolution in the EDZ in unsaturated argillaceous rock with slight modifications. In that study, the strain localisation occurring in the EDZ was taken into account. Other permeability models are parameterised in dependence on pore pressure or stress measures based on the implicit assumption that these quantities determine porosity. Popp et al. [47] presented a semi-logarithmic permeability versus effective pore pressure model. A large number of constitutive models available in the literature consider permeability changes by a direct stress dependence [40, 17, 28, 30, 54]. However, these permeability formulations can not explicitly represent the fact that the permeability change in the EDZ is mainly a consequence of mechanical failure (shear and tensile). Since the choice of a constitutive model is circumstantial, the modeller is often faced with a dilemma: for many applications, an elastic material model may be considered sufficiently accurate for the simulation of coupled THM processes in clay rock. However, the inelastic processes driving porosity and permeability increases in the EDZ can only be captured by advanced constitutive formulations that require a large number of parameters and significant computational resources [45]. In the regions outside the EDZ, such a sophisticated model may not be required.

In the present study, a different approach is therefore explored that relies on a purely elastic analysis but takes into account the degree to which the material is prone to damage locally. For that purpose, a new permeability model is introduced which is a function of a failure index (cf. Section 3.1). This index can be linked to various failure models such as the Mohr-Coulomb or more sophisticated criteria. The new permeability model thus reflects the fact that the permeability change in the EDZ is caused by failure/dilatancy of the COx without explicitly calculating damage.

The purpose of the present study was to numerically simulate the in-situ heater experiments conducted by ANDRA [4] in the COx formation at M/HM URL. In particular, the effects of two constitutive choices introduced into fully coupled THM simulation of the heater experiments were explored: (1) the failure index-dependent permeability model for the EDZ motivated in the previous paragraph, and (2) the advantages of the sophisticated IAPWS density and viscosity models for water. In the numerical simulations, the Galerkin finite element method has been used as implemented in the open-source scientific software platform OpenGeoSys [33, 5]. The numerical simulation took two steps: i) excavation simulation and ii) the heating process simulation with the solutions of the first step as the initial conditions. The study was conducted as a part of Task E of the DECOVALEX 2019 project with a given basic geometry and material properties [50, 51, 46].

Hereafter, the presentation of our work is organised as follows: First, the balance equations of the THM processes that are used for the numerical modelling will be presented in Section 2. Second, the constitutive relationships used will be highlighted including the failure index-dependent permeability model (Section 3.1) and the IAPWS equations of state formulations for water (Section 3.2). Finally, the detailed results of the numerical simulation of the TED experiment within the framework of Task E of the DECOVALEX 2019 project are presented (Section 4) followed by conclusions.

2. Theoretical and numerical methods

In this study, we consider coupled THM processes in fully water-saturated rock, which consists of incompressible solid and slightly compressible water phases.

2.1. Governing equations

Using the concept of the representative elementary volume (REV), one can integrate the microscopic THM equations over the REV domain and obtain the macroscopic balance equations, which are applicable for continuous domains

[35, 19, 31, 52].

Thermal Process

We consider advective and conductive heat transfer in the rock mass, which leads to the heat transport equation

$$(\varrho c_p)^{\text{eff}} \frac{\mathrm{d}_\mathrm{S} T}{\mathrm{d}t} + \varrho_\mathrm{L} c_p^\mathrm{L} \operatorname{grad} T \cdot \mathbf{w}_\mathrm{L} - \operatorname{div}\left(\boldsymbol{\lambda}_T{}^{\text{eff}} \operatorname{grad} T\right) = Q_T \tag{1}$$

with the following effective macroscopic parameters [59, 1]

$$(\varrho c_p)^{\text{eff}} = \phi_\mathrm{F} \varrho_\mathrm{L} c_p^\mathrm{L} + (1-\phi_\mathrm{F}) \varrho_\mathrm{S} c_p^\mathrm{S} \tag{2}$$

$$\boldsymbol{\lambda}_T{}^{\text{eff}} = \phi_\mathrm{F} \boldsymbol{\lambda}_T^\mathrm{L} + (1-\phi_\mathrm{F}) \boldsymbol{\lambda}_T^\mathrm{S} \tag{3}$$

and the Darcy velocity for fluid movement

$$\mathbf{w}_\mathrm{L} = -\frac{\mathbf{k}_\mathrm{L}}{\mu_\mathrm{L}} \left(\operatorname{grad} p - \varrho_\mathrm{L} \mathbf{g}\right) \tag{4}$$

where $\mathrm{d}_\mathrm{S}/\mathrm{d}t$ is the material time derivative operator following the solid phase, L and S stand for, liquid phase and solid phase, respectively; ϕ_F is the porosity, ϱ stands for density, c_p denotes specific isobaric heat capacity, $\boldsymbol{\lambda}_T$ stands for the thermal conductivity tensor, and Q_T is the heat source term.

Hydraulic Process

The pore pressure change due to differential thermal expansion of the involved phases and due to pore volume change in fully saturated rock is described by

$$\beta_\mathrm{s} \frac{\mathrm{d}_\mathrm{S} p}{\mathrm{d}t} - \left[\phi_\mathrm{F} \alpha_T^\mathrm{L} + 3(1-\phi_\mathrm{F}) \alpha_T^\mathrm{S}\right] \frac{\mathrm{d}_\mathrm{S} T}{\mathrm{d}t} + \alpha_\mathrm{B} \operatorname{div} \frac{\mathrm{d}_\mathrm{S} \mathbf{u}}{\mathrm{d}t} + \operatorname{div} \mathbf{w}_\mathrm{L} = Q_H \tag{5}$$

where β_s is the specific storage, $\mathbf{u}$ is the (solid) displacement vector, α_T^L is the volumetric thermal expansion of fluid, α_T^S is the linear thermal expansion of the solid, and Q_H is the sink or source term of the fluid field. The specific storage and the thermal expansion of fluid can either be obtained by taking the rate of change of fluid density with respect to pressure and temperature, respectively, as

$$\begin{aligned} \beta_\mathrm{s} &= \phi_\mathrm{F} \frac{1}{\varrho_\mathrm{L}} \frac{\partial \varrho_\mathrm{L}}{\partial p} + \frac{\alpha_\mathrm{B} - \phi_\mathrm{F}}{K_\mathrm{S}} \\ \alpha_T^\mathrm{L} &= -\frac{1}{\varrho_\mathrm{L}} \frac{\partial \varrho_\mathrm{L}}{\partial T} \end{aligned} \tag{6}$$

or they can be obtained from empirical formulae based on experiments. In the above, K_{S} is the bulk modulus of the solid grains such that

$$\alpha_{\mathrm{B}} = 1 - \frac{K}{K_{\mathrm{S}}} \tag{7}$$

where K is the drained bulk modulus of the porous solid and α_{B} is Biot's coefficient.

Mechanical Process

The quasi-static equilibrium conditions for the mixture of solid and water are given in terms of total stress as

$$\mathrm{div}\boldsymbol{\sigma} + \varrho^{\mathrm{eff}}\mathbf{g} = \mathbf{0} \tag{8}$$

where $\boldsymbol{\sigma} = \boldsymbol{\sigma}^{\mathrm{eff}} - \alpha_{\mathrm{B}} p \mathbf{I}$ is the total stress. Followed by the generalised Hook's law, the effective stress, $\boldsymbol{\sigma}^{\mathrm{eff}}$ is given as

$$\boldsymbol{\sigma}^{\mathrm{eff}} = \boldsymbol{\mathcal{C}} : (\boldsymbol{\epsilon} - \alpha_T^{\mathrm{S}} \Delta T \mathbf{I}) \tag{9}$$

and the effective density given by

$$\varrho^{\mathrm{eff}} = \phi_{\mathrm{F}} \varrho_{\mathrm{L}} + (1 - \phi_{\mathrm{F}}) \varrho_{\mathrm{S}} \tag{10}$$

2.2. Material properties

According to the geological stratification of the M/HM URL site, the material properties of the COx host rock exhibit strong anisotropy determined primarily by the in-plane and out-of-plane directions of the bedding. In the present work, the anisotropic ratios of the intrinsic permeability, heat conductivity and the elastic properties of COx are kept at the values given in task specifications [49]. The bedding plane is being assumed coincident with the horizontal plane.

As shown in Table 1, all material properties correspond to those given in the DECOVALEX Task E specifications [49] except for intrinsic permeability of the COx and the water properties. For permeability characterisation in the EDZ we introduce a new failure criterion-dependent permeability description (Section 3.1), which was used to represent the intrinsic permeability of the COx in the present simulations. The used equation of state for water allows to consider high pressure and temperature conditions. For this reason, the IAPWS models of water was utilised (Section 3.2).

Table 1: Material properties for Task E Step 2

Property	Value	Unit
Fluid		
Density	IAPWS R7-97, $\varrho_w(p, T)$	kg/m^3
Fluid viscosity	IAPWS 2008, $\mu_w(p, T)$	Pa s
Specific heat capacity	$4.28 \cdot 10^3$	J/(kg K)
Thermal conductivity	0.6	W/(m K)
Solid of COx		
Density	2650	kg/m^3
Specific heat capacity	772	J/(kg K)
Thermal conductivity	$\parallel 2.259, \perp 1.4$	W/(m K)
Linear thermal expansion	$1.4 \cdot 10^{-5}$	K^{-1}
Porous medium		
Porosity	0.15	$-$
Intrinsic permeability	$\parallel 2.9 \cdot 10^{-20} \perp 0.8 \cdot 10^{-20}$ with the EDZ model	m^2
Elasticity		
Young's modulus	$\parallel 6 \cdot 10^9 \perp 1.53 \cdot 10^9$	Pa
Poisson's ratio	0.33	-
Biot's coefficient	0.6	-

2.3. *Numerical approach*

We use the finite element method to simulate the coupled THM processes in COx that are mathematically represented by Equations (1), (5) and (8) together with constitutive equations as well as initial and boundary conditions. The standard Galerkin finite element approach is employed to handle the spatial discretisation of the weak forms of the equations. Linear shape functions were used for temperature and pressure, while quadratic shape functions were adopted for the displacements, respectively. The temporal discretisation is performed by using the implicit Euler method with a fixed time step size. The resulting coupled system of algebraic equations is solved by a staggered scheme, i.e. systems of algebraic equations are solved individually by process (Equations (1), (5) and (8)) and linked via an iterative coupling loop in each time step t_i with time step size Δt_i until convergence of the entire system has been achieved (Fig. 1). R1:2

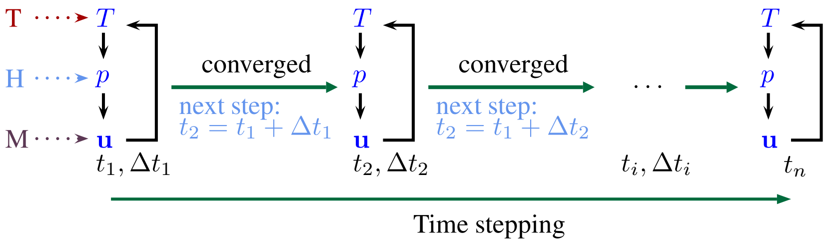

Figure 1: Staggered THM scheme.

R1:2

The numerical THM model is implemented into the OpenGeoSys (OGS-5) open source framework [33, 5].

3. Material behaviour of the EDZ and equations of state for water

In this work we introduce a new model for permeability evolution in the excavation disturbed zone (section 3.1) and use an extended equation of state for water (section 3.2).

3.1. *Permeability model for the excavation damage zone (EDZ)*

The in-situ experiments include drift excavation and micro tunnel drilling. An accurate quantification of the permeability increase in the excavation damage zone (EDZ) is one of the crucial factors to capture the fluid flow during the heating experiments and afterwards for repository operation. Inspired by the fact that the permeability increase in the EDZ is mainly caused by the mechanical failure of rock, we developed a failure index-dependent permeability model for EDZ characterisation that can be used in conjunction with elastic material models as described in the following.

Excavation-induced permeability changes near the drift are an influential factor for an adequate modelling of hydraulic processes in the rock mass during and after excavation [3, 57]. As shown by Pardoen et al. [44] the fluid permeability increases significantly in the vicinity of excavations for Callovo-Oxfordian claystone (Fig. 2). This permeability change is caused by mechanical effects such as damage and dilatancy. Calculating damage and the associated permeability increase explicitly requires constitutive formulations much more involved than elasticity [45], the use of which is not always desired. In contrast, permeability models commonly used for elastic analyses, such as stress or strain-dependent approaches [44, 43], neglect the fact that the change of the permeability in the excavation zone is due to the damage. Here, we explore a novel formulation aiming at a mitigation of this limitation.

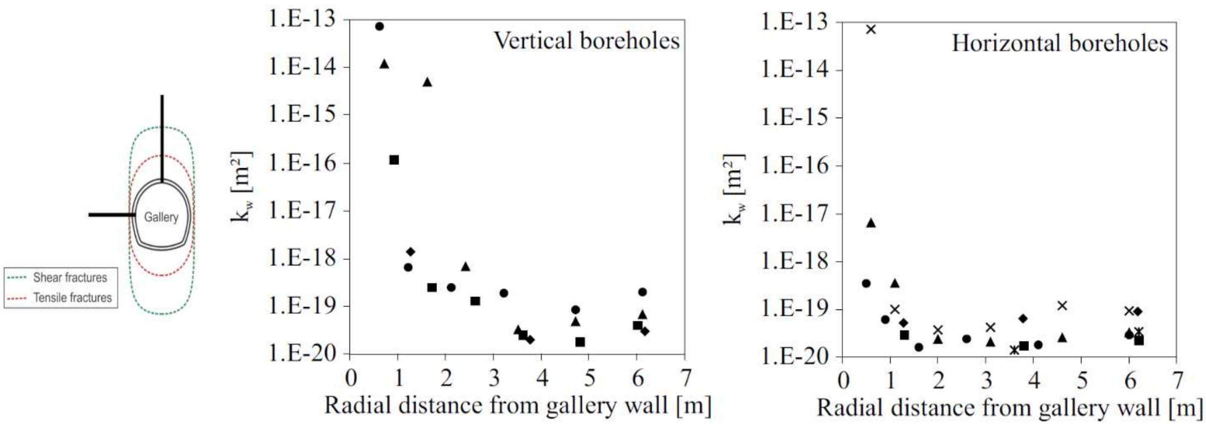

Figure 2: Permeability profile in the near field of a gallery in COx by Pardoen et al. [44]

We hypothesise that the intrinsic permeability $\mathbf{k}$ in the EDZ can be defined as a function of failure index f:

$$\mathbf{k} = \mathbf{k}_0 + H(f-1) k_\mathrm{r} \mathrm{e}^{bf} \mathbf{I} \tag{11}$$

where $\mathbf{k}_0$ is the intrinsic permeability of the undamaged material, H is the Heaviside step function: $H(x) = 0$ for $x < 1$ and $H(x) = 1$ for $x \geq 1$, f is the failure index, k_r is a reference permeability, b is a fitting parameter. k_r and b can be calibrated by experimental data. The failure index f can be calculated from any suitable failure criterion comparing an acting shear stress τ_ff to a strength value τ_f:

$$f = \frac{\tau_\mathrm{ff}}{\tau_\mathrm{f}}, \quad f \geq 1 : \text{failure} \tag{12}$$

The current permeability model is a predictive aid for estimating an excavation-induced permeability increase in the damaged near-contour zone of the excavation. The permeability equation is directly dependent on the stress state. That means if unloading is such that $\tau_\mathrm{ff}/\tau_\mathrm{f}$ reduces, the permeability goes back to k_0. This distinguishes it from a damage model, in which permeability would still be enhanced after unloading (e.g. driven by $\max_t(f-1)$ in the above equation). This prompts that the permeability model can also describe partially reversible permeability change if stress conditions change again to subcritical levels. For example, during the post-closure phase of a repository, due to tunnel convergence and swelling-pressures transferred from the backfill to the tunnel contour, the permeability enhancement of the EDZ is expected to be at least partially reversed [58]. The reversibility aspect of permeability enhancement is still subject to research. Incorporating this as a transient phenomenon into the permeability model was beyond the scope of this study. Instead, we used Equation (11) as an estimator for excavation-induced permeability enhancement here in simulations of heater experiments primarily because of its simplicity and the ability to combine it with different failure criteria.

In the present study, we use a failure index based on the Mohr-Coulomb failure criterion in 3D space:

$$\frac{\sigma_1 - \sigma_3}{2} = \left(\frac{(\sigma_1 + \sigma_3)}{2} \cdot \tan\phi + c\right) \cos\phi$$

where σ_1 and σ_3 are the maximum and the minimum principal stresses, respectively, c is the cohesion and ϕ is the internal friction angle (for clarity, stresses are positive in compression in the above expression with $\sigma_1 \geq \sigma_3$)). Obviously the occurrence of failure can be characterized by the following condition

$$f = \frac{\dfrac{\sigma_1 - \sigma_3}{2\cos\phi}}{\left(\dfrac{(\sigma_1 + \sigma_3)}{2} \cdot \tan\phi + c\right)} \geqslant 1 \tag{13}$$

where $\left(\frac{(\sigma_1 + \sigma_3)}{2} \cdot \tan\phi + c\right)$ is the shear strength τ_{f}, $\frac{\sigma_1 - \sigma_3}{2\cos\phi}$ can be assumed as the acting stress shear stress τ_{ff}, and f can be used as the faliure index of the presented permeability model.

R1:3 and R1:12

~~with~~

$$\tau_{\mathrm{f}} = \left(\frac{(\sigma_1 + \sigma_3)}{2} \cdot \tan\phi + c\right) \cos\phi \quad \text{and} \quad \tau_{\mathrm{ff}} = \tau_{\mathrm{max}} = \frac{\sigma_1 - \sigma_3}{2}$$

Based on the curve given Fig. 2, the parameters of the new permeability model are set as

$$c = 1\,\mathrm{MPa},\ \phi = 15^\circ,\ k_{\mathrm{r}} = 10^{-19}\,\mathrm{m}^2,\ b = 5.5 \tag{14}$$

in the present study.

In order to justify the permeability model, the stress results of the excavation modelling (see Section 4.3) were used. Without loss of generality, we chose a horizontal line on the cross sectional plane extending radially outwards from the drift (see inset in Fig. 3) for an evaluation of the permeability profile. Contour lines of permeability in the EDZ and the failure index along the defined line are plotted in Fig. 3.

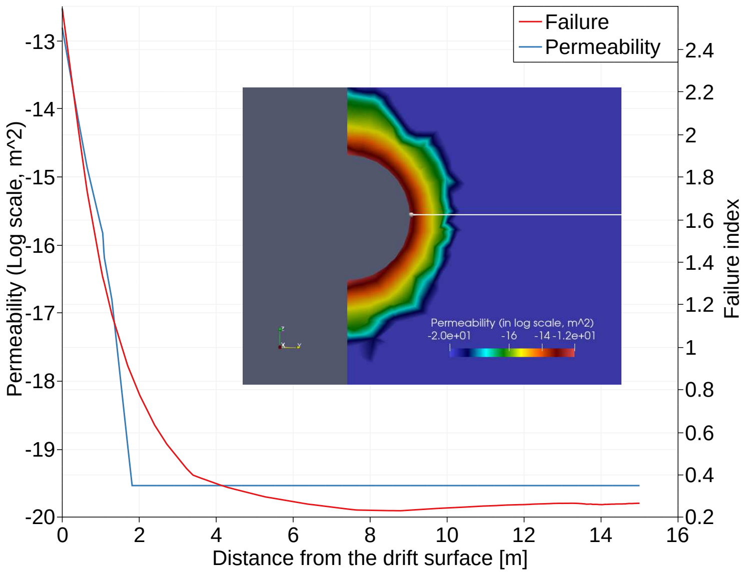

Figure 3: Contour plot of EDZ permeability as well as profiles of permeability and failure index linked by Eq. (11).

One can see that the permeability calculated from the failure index (Fig. 3) is close to the horizontal permeability profile from the experiment which is shown in Fig. 2. The permeability in the vertical direction from the top of the drift is similar to that in the horizontal direction. Note, that here only elastic anisotropy is considered.

3.2. Water properties

During heating experiments or repository operation, water experiences high pressure and temperature changes. The properties of water vary significantly under such changing thermodynamic conditions. There are several equations of state (EOS) available to describe its properties, for example, the linear model [42], the Rowe-Chou equations for water density and dynamic viscosity [48], and the IAPWS equations of state for water density and water viscosity (*Revised Release of the IAPWS Industrial Formulation 1997 for the Thermodynamic Properties of Water and Steam*). Among such water property models, the IAPWS one is precise and has an efficient computational performance in the prediction of thermodynamic properties of pure water under high temperature and pressure. Since the temperature in the study is much less than 623 K, the "region I" formulas of the IAPWS models are utilised. The formula is based on a fundamental equation for the specific Gibbs free energy g, which is expressed in dimensionless form γ as

$$\gamma = \frac{g(p,T)}{RT} = \sum_{i=1}^{34} n_i (7.1-\pi)^{I_i} (\tau - 1.222)^{J_i} \tag{15}$$

where $\pi = p/p^*$, $\tau = T/T^*$ with $p^* = 16.53\,\mathrm{MPa}$ and $T^* = 1386\,\mathrm{K}$, R the specific gas constant, and n_i, I_i, J_i are three sets of constants. The water density is then calculated with as

$$\varrho^w = p^*/(RT\gamma)$$

The water viscosity model uses the formula defined in Release (click here to download the PDF) on the IAPWS Formulation 2008 for the Viscosity of Ordinary Water Substance. In the release note, the viscosity is represented by the equation

$$\bar{\mu} = \bar{\mu}_0(\bar{T})\bar{\mu}_1(\bar{T},\bar{\rho})\bar{\mu}_2(\bar{T},\bar{\rho}) \tag{16}$$

with

$$\bar{\mu}_0(\bar{T}) = \frac{100\sqrt{\bar{T}}}{\sum_{i=0}^{3} \frac{H_i}{\bar{T}^i}},\ H_i \text{ are constants.}$$

and

$$\bar{\mu}_1(\bar{T},\bar{\rho}) = exp\left[\bar{\varrho}\sum_{i=0}^{5}\left(\frac{1}{\bar{T}} - 1\right)^i \sum_{j=0}^{6} H_{ij}(\bar{\varrho}-1)^j\right],\ H_{ij} \text{ are constants.}$$

and $\bar{\mu}_2(\bar{T},\bar{\rho})$ the critical enhancement of the viscosity. In eqn (16), $\bar{\mu}$, $\bar{T}$, $\bar{p}$ and $\bar{\varrho}$ are dimensionless variables defined as

$$\begin{aligned}
&\bar{\mu} = \mu/\mu*, && \mu^* = 10^{-6}\,\mathrm{Pa}\cdot\mathrm{s},\\
&\bar{T} = T/T*, && T^* = 647.096\,\mathrm{K},\\
&\bar{p} = p/p*, && p^* = 22.064\,\mathrm{MPa},\\
&\bar{\varrho} = \varrho/\varrho*, && \varrho^* = 322.0\,\mathrm{kg}\cdot\mathrm{m}^{-3}
\end{aligned}$$

The results obtained from simulations with the IAPWS equations were compared against simulations using the linear model in order to demonstrate the effect of non-linearities in the water's behaviour on coupled THM behaviour (see below). The water density variation due to changes in pore pressure and temperature $\varrho_\mathrm{L}(p,T)$ can be approximated to first order by a Taylor series expansion around a point $\varrho_\mathrm{L}(p_0,T_0)$ giving rise to the linear density model [42]:

$$\begin{aligned}
\varrho_\mathrm{L}(p,T) &\approx \varrho_\mathrm{L}(p_0,T_0) + \frac{\partial \varrho_\mathrm{L}}{\partial p}\Big|_{(p_0,T_0)}(p-p_0) + \frac{\partial \varrho_\mathrm{L}}{\partial T}\Big|_{(p_0,T_0)}(T-T_0)\\
&= \varrho_\mathrm{L}(p_0,T_0)\left(1 + \frac{1}{\varrho_\mathrm{L}(p_0,T_0)}\frac{\partial \varrho_\mathrm{L}}{\partial p}\Big|_{(p_0,T_0)}(p-p_0) + \frac{1}{\varrho_\mathrm{L}(p_0,T_0)}\frac{\partial \varrho_\mathrm{L}}{\partial T}\Big|_{(p_0,T_0)}(T-T_0)\right)
\end{aligned}$$

where for small temperature and pressure increments $\frac{1}{\varrho_\mathrm{L}(p_0,T_0)}\frac{\partial \varrho_\mathrm{L}}{\partial T}|_{(p_0,T_0)} = \alpha_T^\mathrm{L}$ represents the value of the volumetric thermal expansion coefficient of the fluid. The linear model is simple to use but leads to inaccurate results for higher pressure or temperature increments due to its neglect of the non-linear behaviour of water [42]. In contrast, the IF97 water density formula developed by IPWAS represents the non-linear behaviour of the water density to a high degree of accuracy.

In the M/HM URL experiments under investigation, the pore pressure varies in a range of 0.1 MPa to 8 MPa, and temperature ranges from 20 °C to 100 °C or 293 K to 393 K. The parameters of the linear model can be estimated from the IAPWS density model. By setting $p_0 = 1\,\mathrm{MPa}$, we can obtain a curve of $\varrho_\mathrm{L}(p_0, T)$ of the IAPWS density model in the range of $[20, 100]$ °C. As shown in Fig. 4, the corresponding curve of the linear density model takes a straight line between the two ends of the curve by the IAPWS density model. Therefore the temperature related parameter of the linear density model can be obtained as

$$\alpha_T^\mathrm{L} = -\frac{\varrho_\mathrm{L}(p_0, T_b) - \varrho_\mathrm{L}(p_0, T_a)}{(T_b - T_a)\varrho_{\mathrm{L}0}} = 5.568 \cdot 10^{-4}\mathrm{K}^{-1}$$

with $\varrho_{\mathrm{L}0} = 1000\,\mathrm{kg/m^3}$, $T_a = 20$ °C, and $T_b = 100$ °C. Similarly, the pore pressure related parameter of the linear density model is obtained as $\alpha_p^\mathrm{L} \approx 4.54 \cdot 10^{-10}$, $\mathrm{Pa}^{-1}, \forall T \in [20, 100]\,$°C.

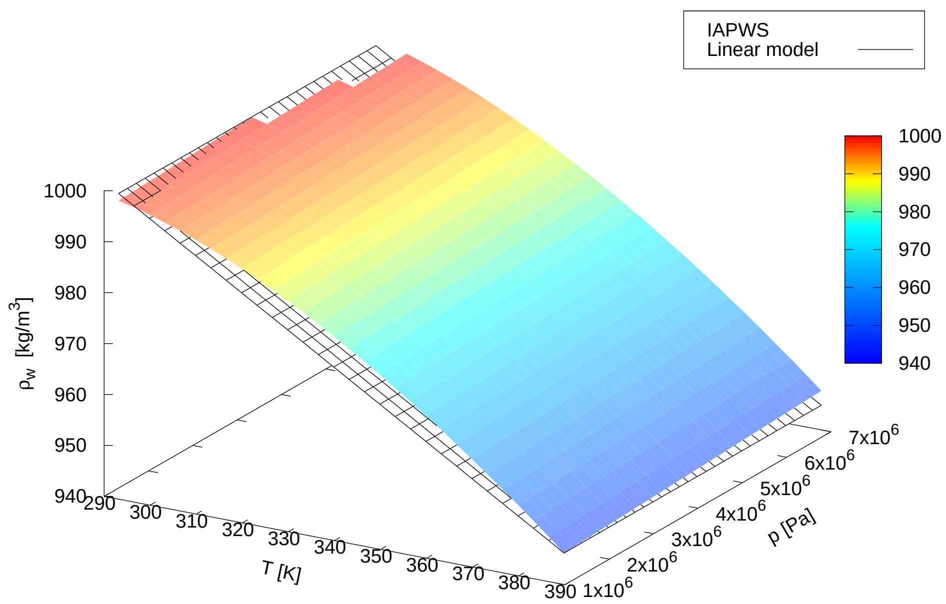

Figure 4: Water density model comparison in a region of $[290, 390]\,\mathrm{K} \times [1, 7]\,\mathrm{MPa}$.

With the obtained parameters of the linear density model, a comparison of the two models in the region of $[290, 390]\,\mathrm{K}\times$ $[1, 7]\,\mathrm{MPa}$ is presented in Fig. 4. It becomes apparent that that two models give a distinct discrepancy both in terms of the density itself and in terms of the orientation of the tangent planes (slopes). The latter represent the thermal expansivity and compressibility of the water phase.

The viscosity of the IAPWS model varies in a range of $1.425 \cdot 10^{-3}$ (Pa s)$^{-1}$ to $1.725 \cdot 10^{-3}$ (Pa s)$^{-1}$ under the present conditions as shown in Fig. 5. A linear viscosity model seems to be appropriate under the current conditions.

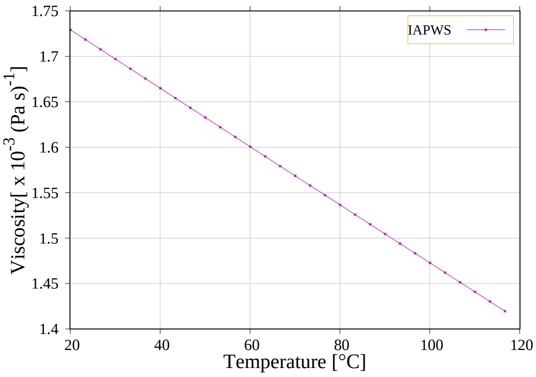

Figure 5: Viscosity of water determined by the IAPWS model.

By simulating the TED heating experiment both with the linear density model and with the IAPWS density and viscosity models, respectively, we investigated the influence of this constitutive choice on the predicted pore pressure fields. In both simulations, all other parameters are kept the same. As shown in the comparison of measured and simulated pore pressures at two~~one~~ of the sensor locations, TED1253_XXX01 and TED1240_PRE02, in Fig. 6, the simulations using the linear density model over predict the pore pressure much more significantly than the simulations using the IAPWS density model. The positions of TED1253_XXX01 and TED1240_PRE02 are depicted in Fig. 7 and Fig. 8b. A simple re-calibration of the linear density model would not only make it more difficult to use than the IAPWS model which can be considered calibrated for a wide range of conditions. It also would be of limited success as long as pressure and temperature conditions largely vary throughout time and space due to the simple fact that it is a mere linearization around one chosen state. Based on this conclusion, the IAPWS formulation was employed in all remaining simulations of the present work.

R1:4

R1:4

4. Modelling of the TED heater experiment

The TED experiment is a small-scale in-situ heating test performed in the Meuse/Haute-Marne Underground Research Laboratory at Bure in France (see also Section 1).

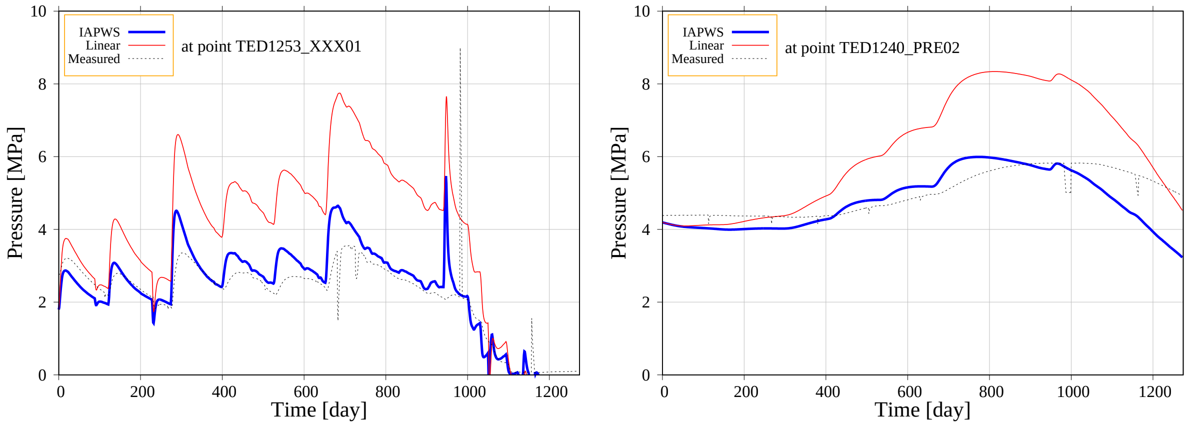

(a) At observation point TED1253_XXX01

(b) At observation point TED1240_PRE02

Figure 6: Comparison of the impact of linear and IAPWS density models on pore pressure predictions at two observation points ~~point~~, TED1253_XXX01 and TED1240_PRE02 ~~(its position is depicted in Fig. 8b)~~.

R1:4

4.1. *Description of the experiment*

The TED experiment is located in the so-called GED drift at a depth of 490 m below the ground surface, and it was started on 25. January 2011 until it was shutdown on 19 July 2013. In the experiment, three heaters were placed in three 25 m separate horizontal micro-tunnels parallel to each other at a distance of 2.7 m and perpendicular to the GED drift. Each micro-tunnel for a heater has a length of 16 m and a diameter of 160 mm, and at the end of which a 4 m long heater was placed. As shown in Fig 7, the experiment site has several boreholes, which were heavily equipped with many sensors [15]. These sensors were used to record the temperature and pore pressure data during the heating experiment. Eleven of these sensors were selected for result comparison.

Among them, six sensors (termed as TED1210_TEM05, TED1219_TEM05, TED1250_TEM01, TED1251_TEM01, TED1253_XXX01, and TED1258_XXX01) are at a distance of 14 m from the GED drift in the plane coinciding with the mid-section of the heaters, which are used for comparison of temperature, pore pressure and displacement results. While the other five selected sensors are only for pore pressure data, and they are located in borehole TED1240 (see Fig. 7), which is almost parallel to the heaters. A cubic domain of $50\,m \times 50\,m \times 50\,m$ was defined for the study. The domain includes the half of the GED drift, heater boreholes, and sensor boreholes. Fig. 8a depicts the domain with its coordinate ranges, while Fig. 8b shows the positions of the selected sensors. The positions of the sensors at borehole TED1240 are shown as a projection on the plane at $y = 14$ m with $(x, z) = (7, -0.01)$. The y coordinates for the sensors at borehole TED1240 are given in Table 2.

Sensor name	PRE01	PRE02	PRE03	PRE04	PRE05
y	19.92 m	13.9 m	10.39 m	7.89 m	4.88 m

Table 2: y coordinate of the five sensors on TED1240 (data from [50]).

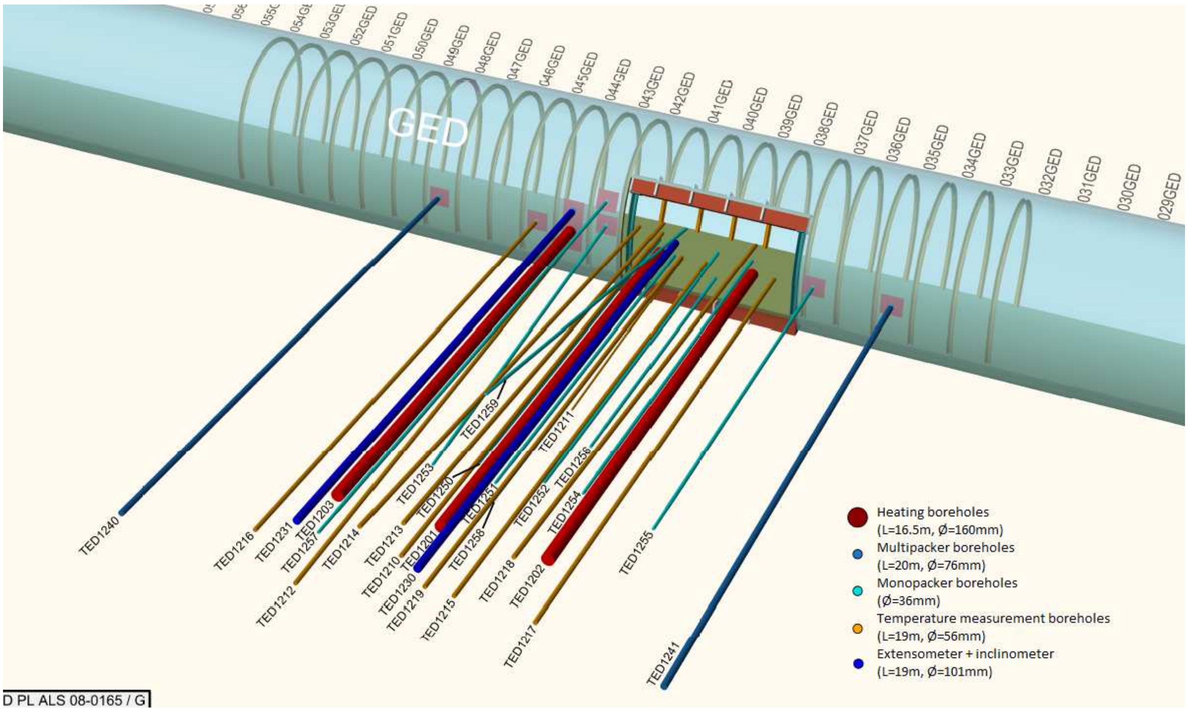

Figure 7: Schematic of the TED experiment (by courtesy of Conil et al. [15]).

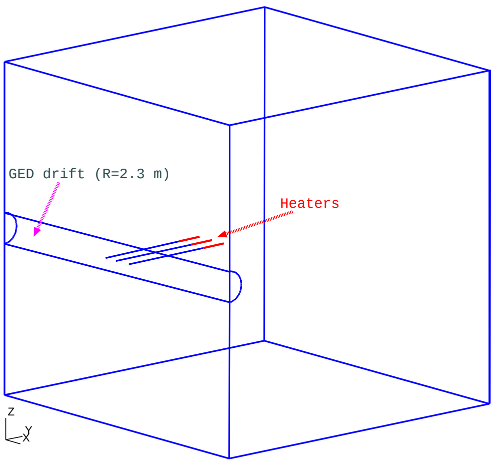

(a) Model domain of the TED experiment: $(x, y, z)^T \in \mathbb{R}^3 : [-25, 25] \times [-2.3, 47.7] \times [-25, 25]$.

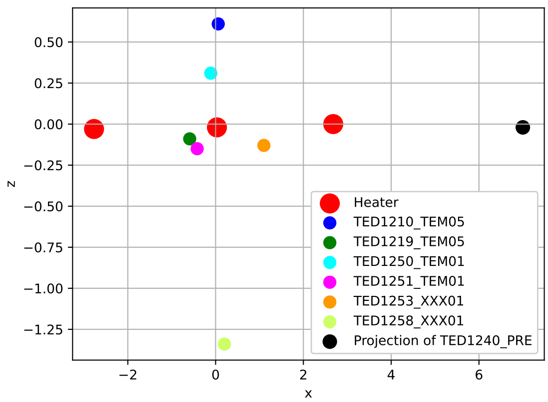

(b) Positions of the six sensors for all variable results (located on the plane at $y = 14$ m), and the projected positions of the sensors for pore pressure results (at borehole TED1240).

Figure 8: Geometry of the domain for study and positions of the selected sensors (data from [50]).

4.2. Numerical model

Recapitulating the construction and operation sequence of the experimental site including instrumentation and the actual heating test, the numerical simulation was split into two successive steps: Excavation and Heating/Cooling phases:

1. Simulation of the excavation based on the initial conditions of $T_0 = 22\,°\mathrm{C}$, $p = 4.7\,\mathrm{MPa}$, $\sigma_\mathrm{h} = -12.4\,\mathrm{MPa}$, $\sigma_\mathrm{H} = -16.1\,\mathrm{MPa}$, and $\sigma_\mathrm{v} = -12.7\,\mathrm{MPa}$ and the excavation timeline of the GED drift as well as the drilling of boreholes in 645 days.

2. Simulation of the coupled THM processes evolving for 1270 days as a consequence of the heating and cooling phases using the results from the excavation simulation.

The finite element method was used to conduct the numerical analysis. The domain shown in Fig. 8a was discretised into 229,732 tetrahedral elements.

4.3. Excavation and instrumentation phase

For simulating the excavation phase, we considered the time period between the beginning of the excavation of the GED drift and the beginning of the heating test. In that period, drilling and the installation of the experimental devices and sensors were included, resulting in a total duration of 664 days. As described in [49], all boreholes were assumed as watertight except the extensometer boreholes (TED1230 and TED1231) and the heater boreholes (TED1201, TED1202 and TED1203). Therefore, we only considered the pore pressure change on the surfaces of the GED drift, extensometer boreholes and the heater boreholes for the excavation modelling. Along with the excavation timeline, the surface of the excavated portion of the GED domain was prescribed with a constant pore pressure of 0.1 MPa and the released traction that is calculated from the initial stress. The extensometer boreholes and the heater boreholes have a relatively small radius, and were thus represented as lines consisting of finite element edges for the 3D finite element method. For these boreholes, the atmospheric pressure of 0.1 MPa was applied as a boundary conditions as soon as their drilling was started and no mechanical boundary condition was prescribed (Table 3). This gives a simplified boundary condition at the heater borehole for the drilling simulation.

Boreholes for sensors and the watertight boreholes were drilled in a short time interval at different times, and were sealed or grouted after drilling [50]. For example, borehole TED1240 was drilled at 6 July 2009 11.50 am. For the boundary boundary condition at these boreholes or sensors at these boreholes, a Dirichlet boundary condition of 0.1 MPa within a two day period was applied as given in Table 3.

The complete set of boundary conditions for the excavation modelling of the TED experiment is given in Table 3.

4.3.1. Simulation results

Since there is no distinct heat source present during the excavation, we only considered the HM coupled processes during the 664 days' excavation, borehole drilling and instrumentation phase.

Table 3: Boundary conditions of the excavation and instrumentation modelling.

Boundary	**T**	**H**	**M**
Front, Rear, Left, Right surfaces	No heat flux	No water flux	No normal displacement
Top surface	T = 21° C	p=4.7 MPa	No traction increment
Bottom surface	T = 23° C	p=4.7 MPa	No normal displacement
GED surface	T = 22° C	Linearly drops from 4.7 MPa to 0.1 MPa in 276 days	Normal traction calculated from the initial stresses
TED1230 & TED1231 (extensometers)	No flux	p=0.1 MPa (t>455 day)	No boundary condition
Heater boreholes: TED1201, TED1202 & TED1203		p=0.1 MPa (TED 1201, t>535 day) (TED 1202, t>539 day) (TED 1203, t>532 day)	
TED1240	No flux	p=0.1 MPa, $t \in [441, 443]$ days	No boundary condition
TED1210		p=0.1 MPa, $t \in [477, 479]$ days	
TED1219		p=0.1 MPa, $t \in [483, 485]$ days	
TED1250		p=0.1 MPa, $t \in [451, 453]$ days	
TED1251 & TED1253		p=0.1 MPa, $t \in [442, 444]$ days	
TED1258		p=0.1 MPa, $t \in [514, 516]$ days	

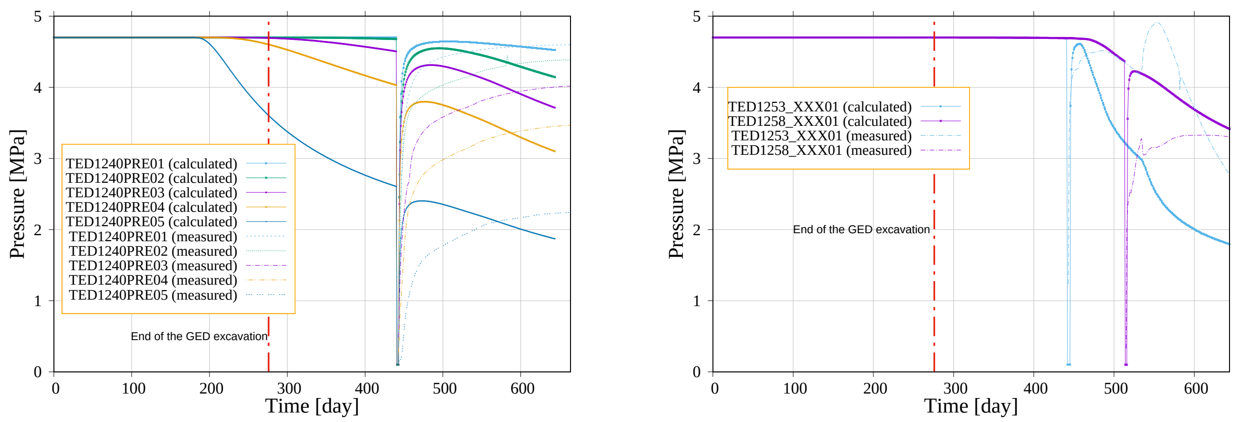

(a) Observation points on TED1240

(b) Observation points on TED1253, TED1258

Figure 9: Pore pressure evolution at the measurement points during the 664 days' excavation and instrumentation time

Fig. 9 compares the measured and calculated temporal pore pressure evolution in five observation points at borehole PRE1240, TED1240PRE01-05. As shown in Fig 9, the excavation deduced pressure drop was captured by the numerical results. However the trends of pore pressure evolution after excavation, when the sensors were installed and their host boreholes were grouted, did not follow that of the measured pore pressure. At the sensor positions, the calculated pore pressures increase immediately in a short time and then slowly decrease. While the measured pore pressures increase monotonically. The reason for such difference can be explained as follows:

- There are many boreholes in the TED experiment site, and only a few of them (heater boreholes and extensometer boreholes) were taken into consideration for their drilling simulation [50].

- Dirichlet boundary conditions of 0.1 MPa for pressure were applied to the measurement points not along the host boreholes.
- The detailed permeability change due to drilling was simplified along with the above simplification of the drilling condition to pore pressures.

Such simplifications in boundary conditions for pore pressures cannot exactly represent the reality of the drilling process. The results show clearly that it is necessary to take into account the impact of the excavation of drift and boreholes on the pore pressure development and therefore did not lead to a numerical solution that could fully match the measurement.In fact, the same evolution behaviour occurs in the numerical results at the sensors near the heaters as that shown in Fig.9b. At the end of the excavation and instrumentation simulation, the values of modelled and measured results at the sensor positions are comparable. Therefore, these results can be used as initial conditions of pore pressures for the heating phase.

Fig. 10 illustrates the variations of the maximum shear stress and normal stress on the maximum shear stress plane at the observation points. As for stress result, we refer stress as effective stress hereafter. The maximum shear stresses at R1:8 the measurement points plotted in Fig. 10a exposes that the excavation of the GED boreholes decreases the maximum shear stress at the measurement boreholes. Fig. 10b proofs that the excavation of GED only leads to a small amount of change in the normal stress on the maximum shear stress plane. ~~Since the sizes of boreholes are relatively small compared to the domain size, the mechanical change caused by drilling can be neglected. Therefore, the condition of drilling was only represented by the pore pressure dropping down to 0.1 MPa in the modelling (Table 3).~~ Fig. 10a R1:7 shows that there is a slightly change of the maximum shear stress at the observation points excecpt at TED1258, which is relative far from the drilled borehoes. However, as shown in Fig. 10b, ~~As shown in Fig. 10b and Fig. 10a,~~ R1:7 significant changes of the normal stress on the maximum shear stress plane during drilling was reproduced by the numerical simulation even with a simplified drilling condition.

Fig. 11 shows the results of pore pressure and vertical stress distributions after the excavation process in the model domain. The calculated vertical stress at the bottom of the GED drift is zero as expected after excavation. The stress changes in the vicinity of the three heating boreholes were captured in the modelling by the hydraulic coupling effect as that there is no mechanical conditions applied at all at the three heaters.

4.4. Heating phase

Analysis of the heating phase uses the results of the excavation and instrumentation phase as initial conditions. The boundary conditions were the same as those used during the excavation and instrumentation phase (cf. Tab. 3) except

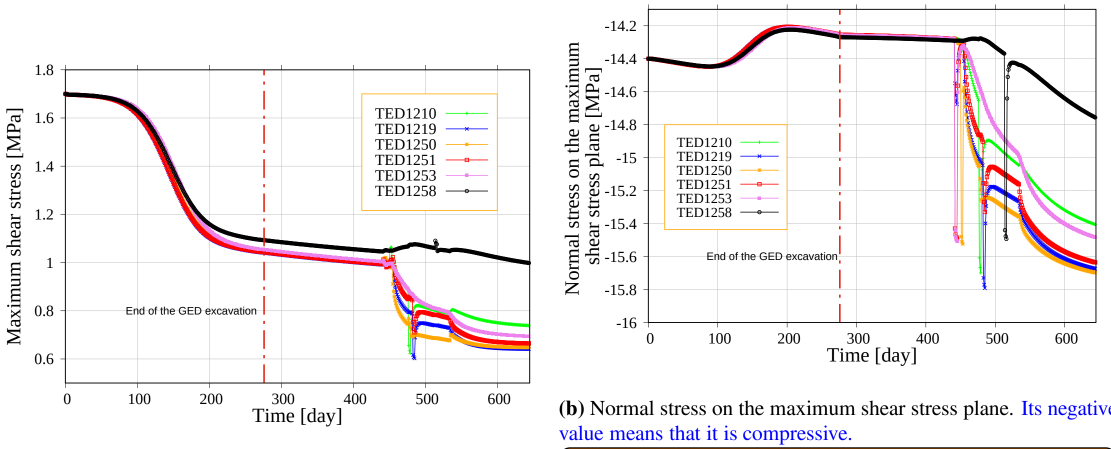

(a) Maximum shear stress, $\tau_{\max}$

(b) Normal stress on the maximum shear stress plane. Its negative value means that it is compressive.

R1:9 (two figures will be aligned once this mark is removed.)

Figure 10: Calculated shear and normal stresses on the maximum shear stress plane at the measurement points during the excavation and instrumentation.

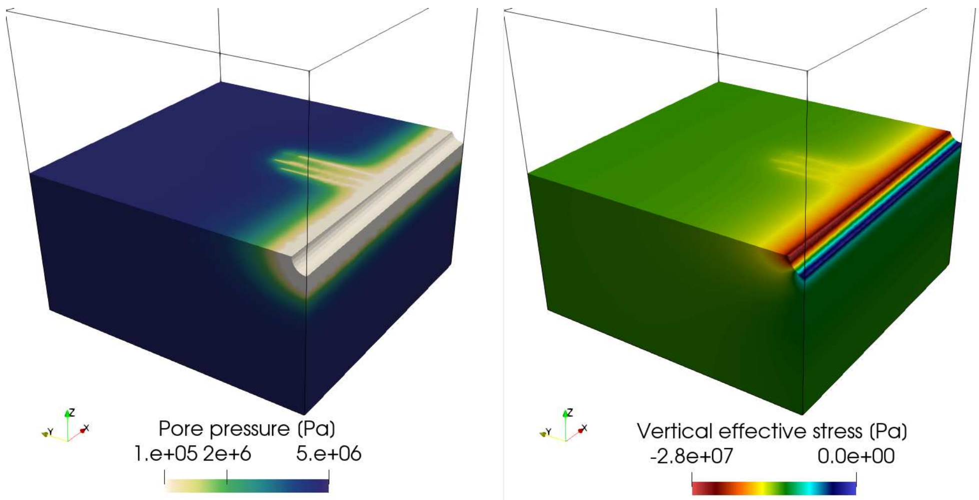

Figure 11: Distribution of pore pressure and vertical stress after excavation

that 1) the heat power curves (Fig.12) [14, 49, 15] were applied to the three lines representing the heaters as Neumann boundary conditions,

2) the atmospheric pressure condition at the watertight boreholes was removed, and 3) a measured temperature curve [14, 49] was applied on the surface of the GED drift as a Dirichlet boundary condition to mimic drift ventilation. Overall, 1271 time steps ($\Delta t = 1d$) were computed for the 1271 days of the heating phase.

The boundary conditions of the heating phase are summarised in Table 4.

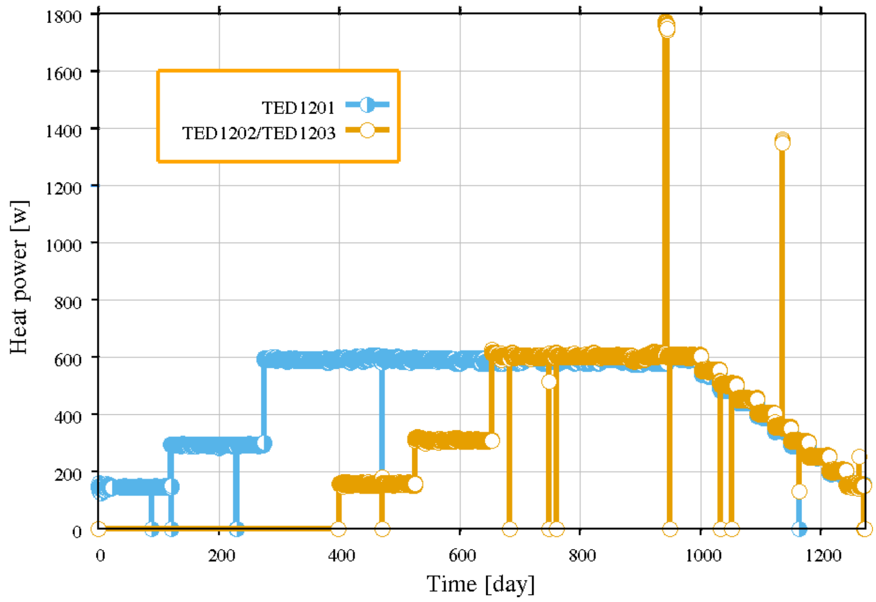

Figure 12: Heat power curve (data from Conil et al. [14], Seyedi et al. [49], Conil et al. [15])

Table 4: Boundary conditions for the heating modelling of TED experiment

Boundary	T	H	M
Front, Rear, Left, Right surfaces	No heat flux	No water flux	No normal displacement
Top surface	$T = 21\,^{\circ}\mathrm{C}$	$p = 4.7\,\mathrm{MPa}$	No traction increment
Bottom surface	$T = 23\,^{\circ}\mathrm{C}$	$p = 4.7\,\mathrm{MPa}$	No normal displacement
GED surface	Measured temperature [14, 49]	p = 0.1 MPa	Free traction
TED1230 & TED1231 (extensometers)	No flux	p = 0.1 MPa	No boundary condition
Heater boreholes: TED1201, TED1202 & TED1203	Heat power [14, 49]	p = 0.1 MPa	

4.4.1. *Thermal process*

Fig. 13a displays the temperature evolution at the measurement points of TED1210, TED1219, TED1250 and TED1251 from the start of the heating phase. It can be seen from Fig. 13a that the numerical results and the measured ones at these four points are in a good agreement. This holds for both the heating and the cooling phases. These four points are close to the central heater within a distance of 0.61 m. In contrast, the points TED1253 and TED1258 are 1.14 m and 1.36m far from the heaters, respectively, and their measured temperature data history is incomplete. As shown in Fig. 13b, the computed temperatures at these points is overestimated as the temperature variation approaches its peak value. Excluding the measurement error, such numerical overestimation at the points TED1253 and TED1258 can come from the inaccuracy of the computed pressure field. As addressed in the following content, the pressure of the experiment, especially in the far field, can not be well reproduced (see Fig. 14) by the numerical modelling due to that the complex boundary conditions of the boreholes and outer surfaces were simplified. Compared to the other observation points, the thermal advection has more influence at TED1253 and TED1258, which have more large distance from the heaters. R1:10

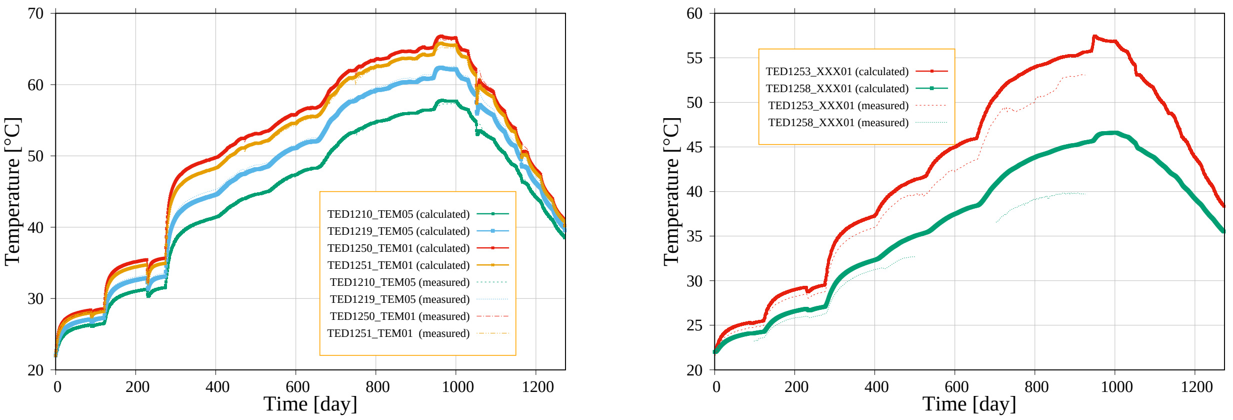

(a) Points of TED1210, TED1219, TED1250, TED1251 **(b)** Points of TED1253, TED1258

Figure 13: Temperature evolution at the measurement points.

4.4.2. Hydraulic process

During the excavation and the instrumentation phases, hydraulic processes are only driven by the excavation operations. Conversely, after the commencement of heating, the main source driving the hydraulic process is the temperature change. The temperature change decreases the water density, i.e. leads to thermal expansion in the fluid which exceeds the expansion of the pore space due to solid thermal expansion and thus eventually results in a local pore pressure increase.

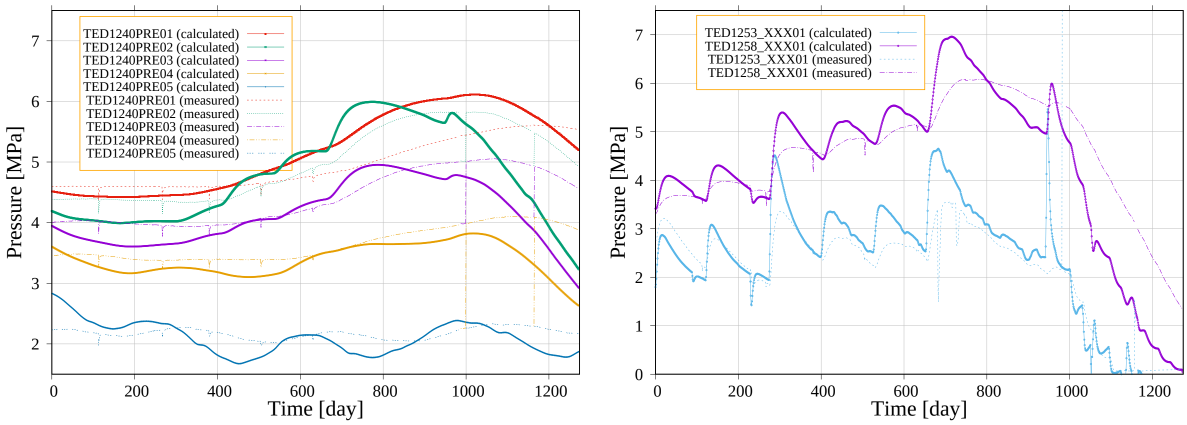

(a) Observation points of TED1210, TED1219, TED1250, TED1251 **(b)** Observation points of TED1253, TED1258

Figure 14: Pore pressure evolution at the indicated measurement points

Fig. 14 shows the pore pressure variation at the specified measurement points. Although the evolution trends as well as the magnitudes are similar between the measured and simulated pore pressure, some discrepancies remain. The magnitude of these discrepancies is similar regardless of the positions of the measurement points. Points of TED1253, TED1258 are much closer to the heaters than that of points on borehole 1240, where the pore pressure varies significantly along with the variation of the heat power. Fig. 14b shows that the numerical results at points of TED1253, TED1258 roughly reproduced the fluctuation of the measured pore pressure data. The reason of the discrepancy in the calculated and measured pore pressure values can have various reasons: (i) simplified boundary conditions as discussed previously in relation to Fig. 9, (ii) effect of elevated hydraulic properties, e.g. by heterogeneity, and/or (iii) compressibilities. Furthermore, the values are neither consistently over-predicted nor under-predicted.

4.5. *Mechanical process*

As there are no measured data available for the mechanical process, only the obtained numerical results will be presented and discussed on their plausibility.

The temporal variation of the mechanical variables at the specified points are plotted in Figs. 15. Fig. 15a shows that thermally induced displacements during the heating test are small. The maximum displacement magnitude at the specified points, which are close to heaters, is less than 1.7 mm. Fig. 15b illustrates that among the specified points, TED1251 experienced the maximum shear stress during the heating test. These stress results capture the fact that TED1251 is near to the central heater. The stress change there should be larger than that at the other specified points. Fig. 15c also depicts that the maximum stress change is around 4 MPa. Although the magnitude of the stress change is large, the variation of maximum shear stress keeps in a small range as shown in Fig. 15b. The corresponding failure index under the present failure criterion is in the safe regime (Fig. 15d). R1:11

For more details, we provide cross-sectional plots at a vertical plane cutting the centres of the three heaters. Fig. 16 displays the distributions of the maximum shear stress ($(\sigma_3 - \sigma_1)/2$) and the normal stress on the maximum shear stress plane ($(\sigma_3 + \sigma_1)/2$) at day 950. Fig. 16 shows that in a small area around the heaters the highest magnitude of stress changes occurs. This means that if failure occurs during the heating process, it may occur in the vicinity of the heaters.

However, the drilling damage zones of the heater boreholes are ignored because the radii of the heater borehole are relatively small and therefore do not affect the remaining domain appreciably.

Fig. 17 visualises the distribution of the increments of THM variables from the initial state until 400 days, 950 days, and 1200 days of heating, respectively. ~~950 days of heating, when the temperature almost reaches its maximum value.~~ R1:14

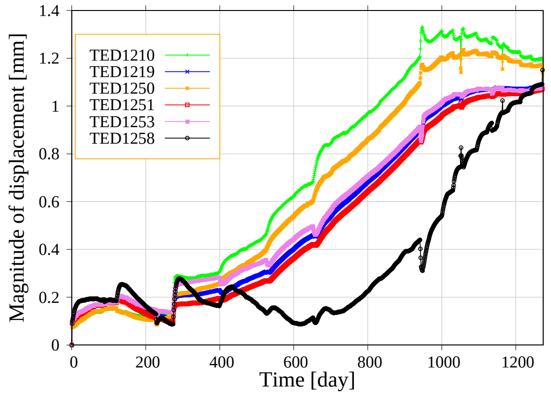

(a) Displacement magnitude, $\|\mathbf{u}\|$

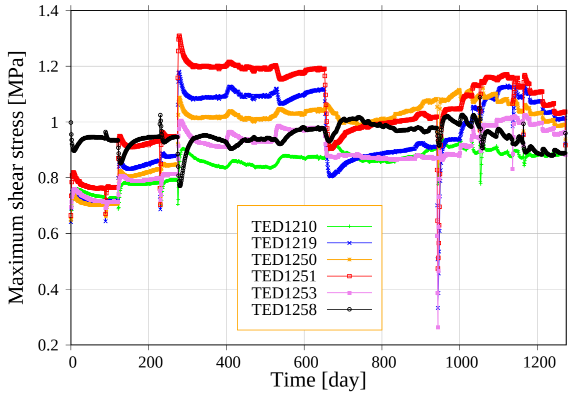

(b) Maximum shear stress, $\tau_{\max}$

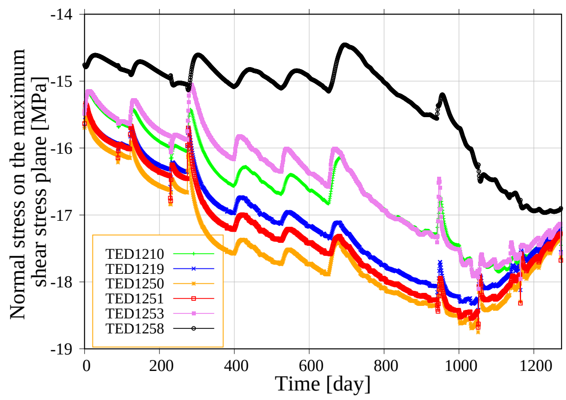

(c) Normal stress on the maximum shear stress plane. Its negative value means that it is compressive.

R1:9 (two figures will be aligned once this mark is removed.)

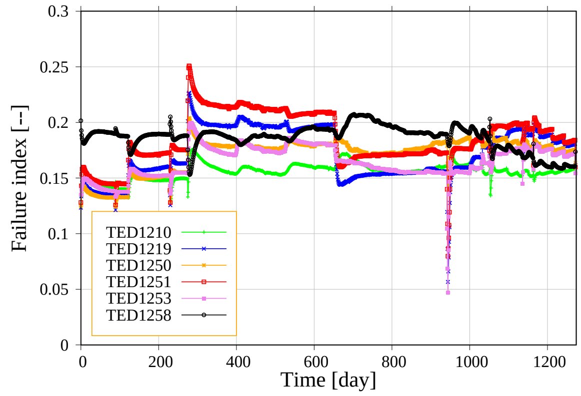

(d) Failure index

Figure 15: Variations of the variables of mechanical process at the measurement points.

R1:14

Before 400 days, only the middle heater provides the heat power. The temperature distribution in Fig. 17a shows that the other two heaters just started heating at 400 days, which as also shown in Fig. 17a increases the pore pressure and the stress magnitude near the two heaters immediately. In the vicinity of the middle heater, the pore pressure has already been driven down to the air pressure boundary condition at the heater by the 400 day's thermal expansion. As shown in Fig. 17b, the temperature almost reaches its maximum value at all the three heaters after 950 days of heating. Associated with the highest temperature change, the highest pressure increment occurs in a large domain surround the three heaters even the water can flow out along the heaters under an assumption of a constant pressure of 0.1 MPa. Without the exception, the maximum stress increment occurs at the heater boreholes as shown in Fig. 17b. At 1200 days since the heating, the heat power is in an attenuation state, as a consequence the changed THM variables are

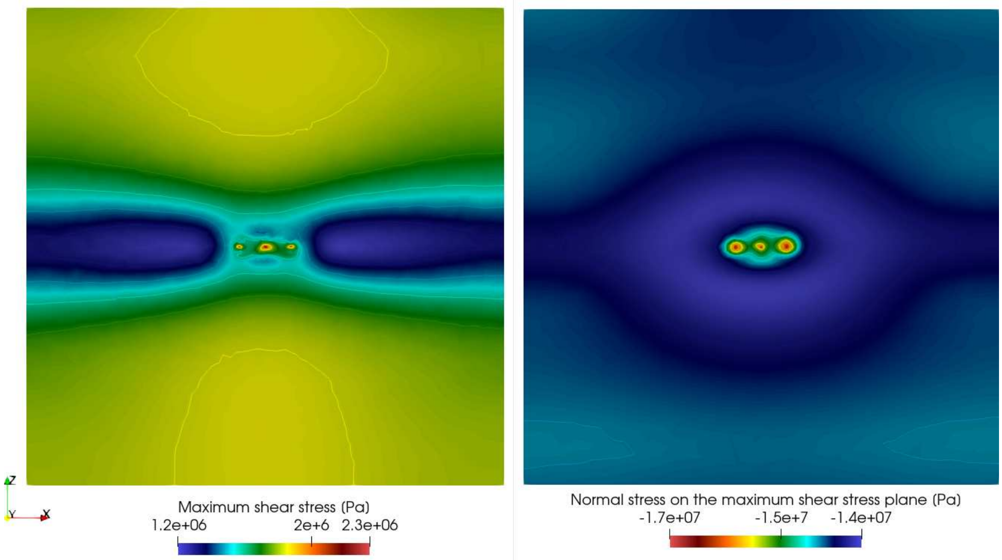

Figure 16: Distributions the maximum shear shear stress (left figure) and its associated normal stress (right figure) at 950 days on a vertical cross section (50 m × 50 m)

R1:13

in the heater borehole direction and at the depth of 12 m in the heater borehole.

recovering to the their initial status. This trend can be identified by comparing Fig. 17c and Fig. 17b. Fig. 17 gives an impression of the extent of the area affected by the temperature variations. Obviously, high pressures and stresses occur in the region around the heaters, where the thermal expansion is highest. The draining boreholes are also clearly visible as low-pressure areas. This visualisation highlights the importance of THM coupling effects in the context of heat-emitting waste deposition.

In the present study, stresses also play a critical role in the permeability change via the failure index as that described in Section 3.1. Fig. 18 displays the distributions of the failure index and the permeability at 950 days on a vertical cross section containing the centre heater. Since the GED drift has a far distance from the heaters, and water is allowed to drain out from the GED surface through the damage zone, the stress field in the vicinity of the the GED drift exhibits only small changes after the excavation process. Therefore, in that area the failure index as well as its associated permeability reduction by the presented permeability model remains almost unchanged from the post excavation status as shown in Fig. 3 and Fig.18. The permeability reduction in the EDZ flattens the pore pressure R1:15 increment driven by the thermal expansion of water. Without the consideration of the permeability reduction in the EDZ, the computed pressures at the measurement points would be larger than that are shown in Fig. 14. In the vicinity of the heaters, the stress changes are mainly caused by thermal expansion, which results in smaller shear stresses. Therefore, the failure index there is smaller than 1 as depicted in Fig. 18, and consequently there is no permeability change predicted in the vicinity of the heaters by the present numerical simulation.

5. Conclusions

In this paper, a numerical study of coupled thermal-hydro-mechanical (THM) processes during an in situ heater experiment in Callovo-Oxfordian clay rock, the TED experiment conducted by ANDRA [4], is presented. The excavation damage zone (EDZ) in the site was investigated in detail by Pardoen et al. [44]. To better describe THM processes in the EDZ, which is highly affected by permeability reduction, a mechanical failure index dependent permeability model was introduced. The model was justified against the permeability profile in the EDZ in Callovo-Oxfordian claystone by Pardoen et al. [44]. Since the presented permeability model is based on stress changes, the new approach can also describe the permeability recovery in the closure process of drifts or boreholes. The properties of water exhibit distinct nonlinear variation under high temperature and pressure. We employed the IAPWS density and viscosity models to more precisely represent such water behaviour in the heated Callovo-Oxfordian claystone.

The main outcomes for presented THM analyses and related suggestions can be summarised as follows

Thermal processes: Good agreement between calculated results and measured data was achieved at all sensor locations in the vicinity of the heaters (< 1m). The overestimation at the two sensors TED1253 and 1258 (about one meter from the heaters) may be due to measurement uncertainty or variations in the thermal conductivity. In this case, possibly an unsaturated zone in the near-field should be considered, additional measurements are recommended to clarify this.

Hydraulic processes: At the selected observation points, the obtained pore pressure recovery variations after the excavation and the borehole drilling cannot exactly follow the temporal measurements. The reason behind is that the pore pressure boundary conditions were applied only at few selected boreholes or even at the selected sensor points on the boreholes. Such simplifications of pore pressure boundary conditions cannot fully represent the pore pressure field during excavation - due to the fact that the experimental site has many boreholes. At the end of excavation and instrumentation's, the obtained pore pressure values are close to the measured ones again and, therefore, can server well as initial conditions for the subsequent heating/cooling phases. During the heating stage, the simulated pore pressure results capture the measured values in their temporal evolution and magnitude very well with the help of the presented permeability model and the IAPWS water models.

Mechanical processes: As there were no mechanical measurement data available, the evaluation is based on plausibility and the comparison against other modeling teams Task E of the DECOVALEX 2019 project [51] which justifies the obtained numerical results in the presented study. Moreover, the permeability profile and distribution obtained with the new failure index dependent permeability model prompts that obtained stress distribution after excavation is reasonable. The importance of THM coupling effects could be clearly demonstrated and should be taken into account for related safety analyses.

Accounting for the non-linear dependence of water density on pressure and temperature as well as for the temperature-dependence of viscosity significantly improves pressure predictions. Using the IAPWS formulation requires no extra parameters and provides a highly accurate equation of state for water. The permeability changes in the EDZ have represented by introducing a failure index criterion into elastic simulations. Thus, for a first approximation, damage does not need to be calculated by sophisticated material models. Furthermore, the permeability model can be combined with a wide range of failure criteria. Accounting for the permeability enhancement resulted in better findings of the computed pore pressure results at the measurement points for the TED experiment.

Remaining discrepancies, particularly between the calculated and measured pressure data, may be attributed to the following aspects: (i) material properties were assumed to be homogeneous, (ii) not all boreholes were considered in the modelling of excavation, this would extremely complicate numerical simulation due to according mesh requirements, (iii) the closed model domain (no flux boundary conditions on the sides) will suppress water supply in the excavation phase and the cooling stage of the heating test, (iv) the presence of small amounts of gases can change water compressibility drastically and hence alter the pressure transients. Further research is required to resolve those open questions.

For further discussion, comparison results of all participating modelling teams of Task E of DECOVALEX 2019 please refer to the synthesis paper Seyedi et al. [51].

Acknowledgements

DECOVALEX is an international research project comprising participants from industry, government and academia, focusing on the development of understanding, models and codes in complex coupled problems in sub-surface geological and engineering applications. DECOVALEX 2019 is the current phase of the project. The authors appreciate and thank the DECOVALEX 2019 Funding Organisations Andra, BGR/UFZ, CNSC, US DOE, ENSI, JAEA, IRSN, KAERI, NWMO, RWM, SÚRAO, SSM and Taipower for their financial and technical support of the work described in this paper. The statements made in the paper are, however, solely those of the authors and do not necessarily reflect those of the Funding Organisations. The work of BGR was supported by BMWi (Bundesministerium für Wirtschaft und Technologie, Berlin). This study was also partly supported by the German Federal Ministry of Education and Research (BMBF) (GeomInt project, grant number 03G0866A) and Helmholtz Association (iCROSS project, grant numbers 02NUK053E and SO-093) - which is greatly acknowledged. This work is also co-financed within the framework of EURAD, the European Joint Programme on Radioactive Waste Management (Grant Agreement No 847593) which is gratefully acknowledged. We would like to express our thanks to the community of developers and users of the described software, in particular to those involved in the long-term projects OpenGeoSys (OGS), in which the authors are involved. We thank the Helmholtz Centre for Environmental Research – UFZ for long-term funding and continuous support of the OpenGeoSys initiative. OGS has been supported by various projects funded by Federal

Ministries (BMBF, BMWi) as well as the German Research Foundation (DFG).

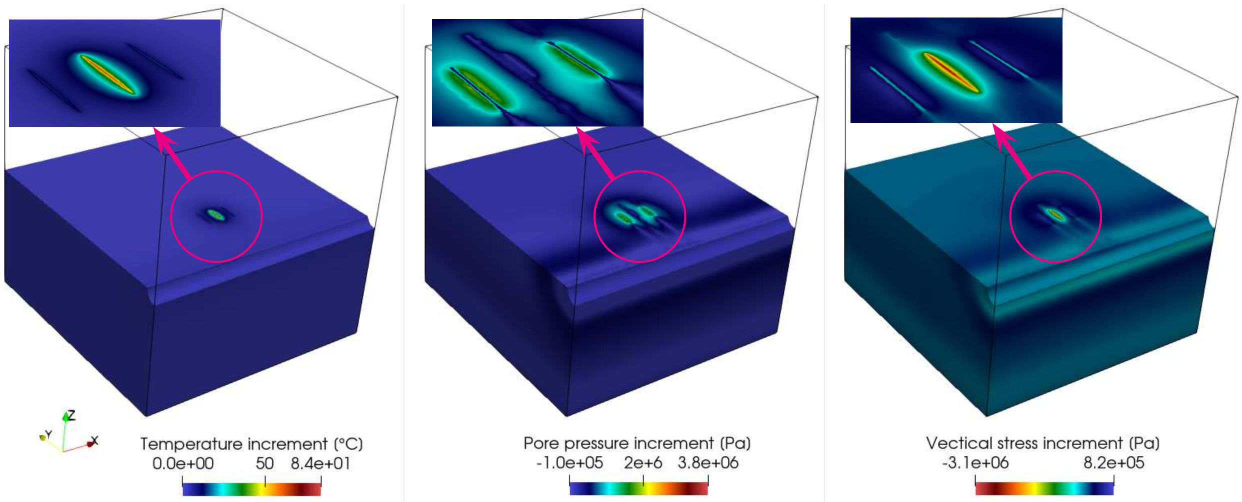

(a) 400 days

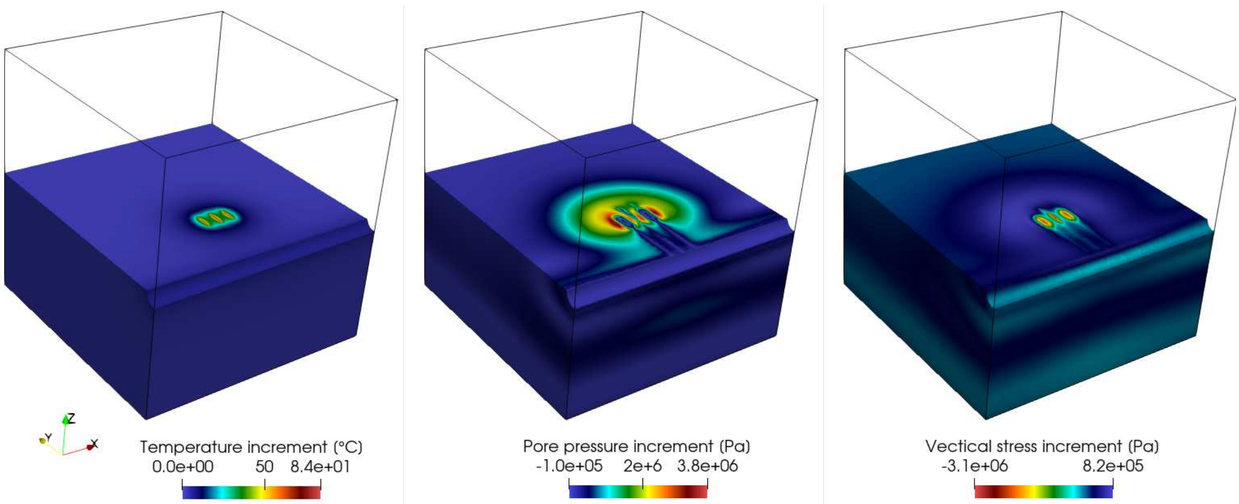

(b) 950 days

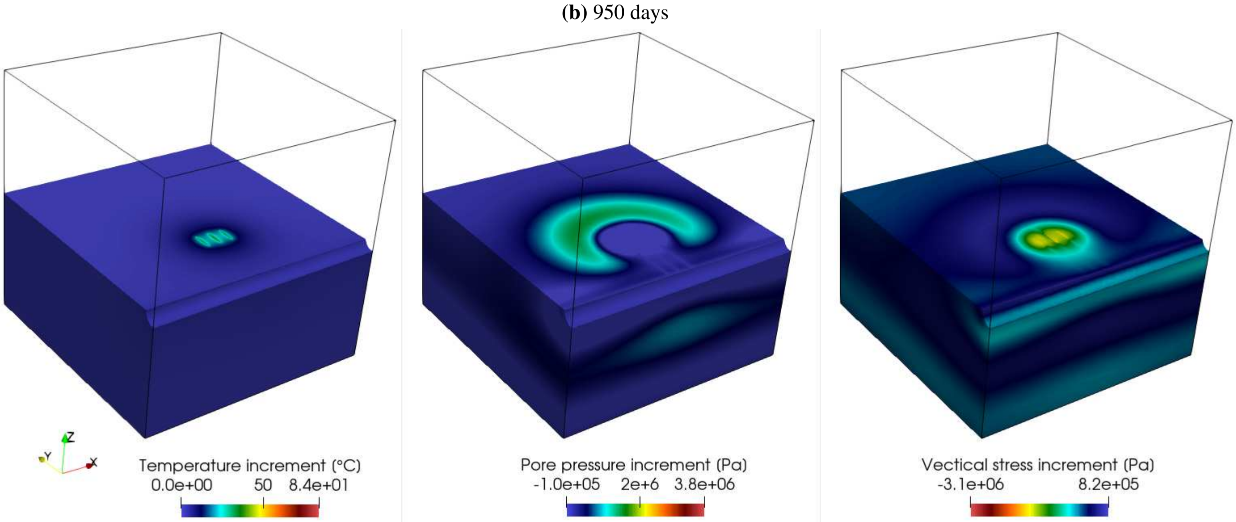

(c) 1200 days

Figure 17: Distribution of the increments of temperature, pore pressure and vertical stress from the initial state: Inside view after 400, 950, and 120 days, respectively, since the heating started.

R1:14

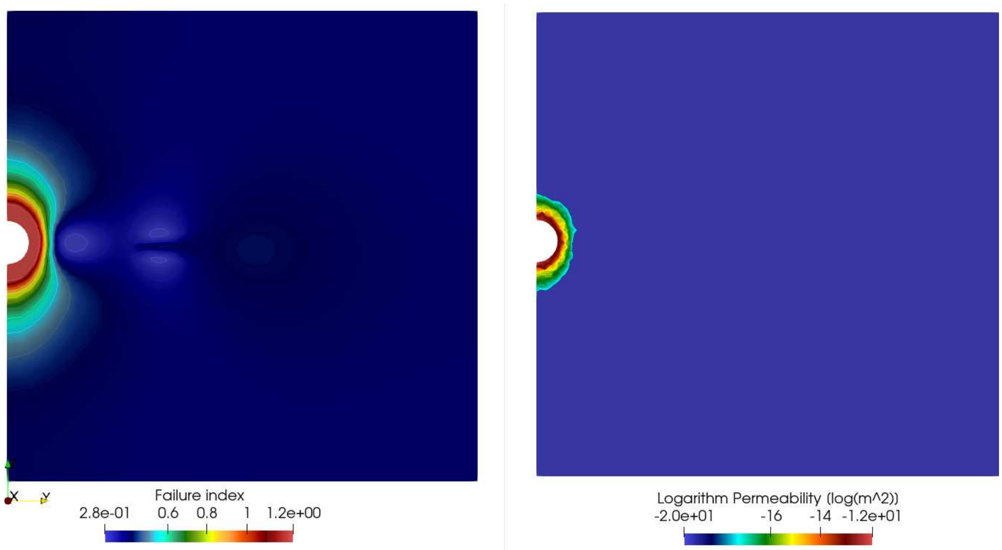

Figure 18: Failure index (left) and permeability distributions (right) at 950 days on a vertical cross section containing the centre heater (50m × 50 m).

R1:13

References

References

[1] M.G. Alishaev, I.M. Abdulagatov, and Z.Z. Abdulagatova. Effective thermal conductivity of fluid-saturated rocks. experiment and modeling. *Engineering Geology*, 135-136:24–39, 2012. doi: 10.1016/j.enggeo.2012.03.001. URL https://www.scopus.com/inward/record.uri?eid=2-s2.0-84860307859&doi=10.1016%2fj.enggeo.2012.03.001&partnerID=40&md5=df1d14f549610ad5f4a79ba72afc28af.

[2] G. Armand, A. Noiret, J. Zghondi, and D.M. Seyedi. Short- and long-term behaviors of drifts in the Callovo-Oxfordian claystone at the Meuse/Haute-Marne Underground Research Laboratory. *Journal of Rock Mechanics and Geotechnical Engineering*, 5(3):221–230, 2013.

[3] G. Armand, F. Leveau, C. Nussbaum, R. De La Vaissiere, A. Noiret, D. Jaeggi, P. Landrein, and C. Righini. Geometry and properties of the excavation-induced fractures at the Meuse/Haute-Marne URL drifts. *Rock Mechanics and Rock Engineering*, 47(1):21–41, 2014.

[4] G. Armand, F. Bumbieler, N. Conil, R. de la Vaissière, J.-M. Bosgiraud, and M.-N. Vu. Main outcomes from in situ thermo-hydro-mechanical experiments programme to demonstrate feasibility of radioactive high-level waste disposal in the Callovo-Oxfordian claystone. *Journal of Rock Mechanics and Geotechnical Engineering*, 9(3):415–427, 2017.

[5] L. Bilke, B. Flemisch, T. Kalbacher, O. Kolditz, R. Helmig, and T. Nagel. Development of open-source porous media simulators: Principles and experiences. *Transport in Porous Media*, 130(1):337–361, 2019. doi: 10.1007/s11242-019-01310-1.

[6] J. R. Booker and C. Savvidou. Consolidation around a point heat source. *International Journal for Numerical and Analytical Methods in Geomechanics*, 9(2):173–184, 1985.

[7] P. Bossart. Twenty years of research at the Mont Terri rock laboratory: what we have learnt. *Swiss Journal of Geosciences*, 110(1):405–411, 2017.

[8] P. Bossart, D. Jaeggi, and C. Nussbaum. Experiments on thermo-hydro-mechanical behaviour of Opalinus Clay at Mont Terri rock laboratory, Switzerland. *Journal of Rock Mechanics and Geotechnical Engineering*, 9(3):502–510, 2017.

[9] Paul Bossart, Peter M Meier, Andreas Moeri, Thomas Trick, and Juan-Carlos Mayor. Geological and hydraulic characterisation of the excavation disturbed zone in the opalinus clay of the mont terri rock laboratory. *Engineering Geology*, 66(1-2):19–38, 2002.

[10] P. Carman. Fluid flow through a granular bed. *Transactions of the Institution of Chemical Engineers*, 15:150–167, 1937.

[11] R. Charlier, F. Collin, B. Pardoen, J. Talandier, J.-P. Radu, and P. Gerard. An unsaturated hydro-mechanical modelling of two in-situ experiments in Callovo-Oxfordian argillite. *Engineering Geology*, 165:46–63, 2013.

[12] A.A. Chaudhry, J. Buchwald, O. Kolditz, and T. Nagel. Consolidation around a point heat source (correction and verification). *International Journal for Numerical and Analytical Methods in Geomechanics*, 2019. doi: 10.1002/nag.2998.

[13] C Chavant and R Fernandes. Evaluating the reliability of hydro-mechanical simulation: a benchmark of numerical techniques carried out by research group of momas. In *2nd International Meeting Clays in Natural & Engineered Barriers for Radioactive Waste Confinement, Tours*, pages 249–250, 2005.

[14] N. Conil, C. Vittel, C. Plua, M.N. Vu, D. Seyedi, and G. Armand. In situ investigation of the thm behavior of the callovo oxfordian claystone. *Journal of Rock Mechanics and Rock Engineering*, 2019. submitted.

[15] N Conil, V Manon, C Plúa, M.N. Vu, D. Seyedi, and G Armand. In situ investigation of the THM behavior of the Callovo-Oxfordian claystone. *Rock Mechanics and Rock Engineering*, 47(1):111–129, 2020. doi: https://doi.org/10.1007/s00603-020-02073-8.

[16] Antonio Costa. Permeability-porosity relationship: A reexamination of the kozeny-carman equation based on a fractal pore-space geometry assumption. *Geophysical research letters*, 33(2), 2006.

[17] J.P. Davies and D.K. Davies. Stress-dependent permeability: characterization and modeling. volume 2, page SIGM/, 1999.

[18] R. de La Vaissière, G. Armand, and J. Talandier. Gas and water flow in an excavation-induced fracture network around an underground drift: A case study for a radioactive waste repository in clay rock. *Journal of Hydrology*, 521:141–156, 2015.

[19] W. Ehlers and J. Bluhm. *Porous Media: Theory, Experiments and Numerical Applications*. Springer, 2002. ISBN 978-3-662-04999-0.

[20] C.P. Enssle, M. Cruchaudet, J. Croisé, and J. Brommundt. Determination of the permeability of the Callovo-Oxfordian clay at the metre to decametre scale. *Physics and Chemistry of the Earth*, 36(17-18):1669–1678, 2011.

[21] S. Escoffier, F. Homand, A. Giraud, N. Hoteit, and K. Su. Under stress permeability determination of the Meuse/Haute-Marne mudstone. *Engineering Geology*, 81(3):329–340, 2005.

[22] B. Garitte, T.S. Nguyen, J.D. Barnichon, B.J. Graupner, C. Lee, K. Maekawa, C. Manepally, G. Ofoegbu, B. Dasgupta, R. Fedors, P.Z. Pan, X.T. Feng, J. Rutqvist, F. Chen, J. Birkholzer, Q. Wang, O. Kolditz, and H. Shao. Modelling the Mont Terri HE-D experiment for the thermal-hydraulic-mechanical response of a bedded argillaceous formation to heating. *Environmental Earth Sciences*, 76(9), 2017.

[23] B. Garitte, H. Shao, X.R. Wang, T.S. Nguyen, Z. Li, J. Rutqvist, J. Birkholzer, W.Q. Wang, O. Kolditz, P.Z. Pan, X.T. Feng, C. Lee, B.J. Graupner, K. Maekawa, C. Manepally, B. Dasgupta, S. Stothoff, G. Ofoegbu, R. Fedors, and J.D. Barnichon. Evaluation of the predictive capability of coupled thermo-hydro-mechanical models for a heated bentonite/clay system (HE-E) in the Mont Terri Rock Laboratory. *Environmental Earth Sciences*, 76(2), 2017.

[24] Benoit Garitte, Antonio Gens, Jean Vaunat, and Gilles Armand. Thermal conductivity of argillaceous rocks: determination methodology using in situ heating tests. *Rock mechanics and rock engineering*, 47(1):111–129, 2014.

[25] B.J. Graupner, H. Shao, X.R. Wang, T.S. Nguyen, Z. Li, J. Rutqvist, F. Chen, J. Birkholzer, W. Wang, O. Kolditz, P.Z. Pan, X.T. Feng, C. Lee, K. Maekawa, S. Stothoff, C. Manepally, B. Dasgupta, G. Ofoegbu, R. Fedors, J.D. Barnichon, E. Ballarini, S. Bauer, and B. Garitte. Comparative modelling of the coupled thermal–hydraulic-mechanical (THM) processes in a heated bentonite pellet column with hydration. *Environmental Earth Sciences*, 77(3), 2018.

[26] Lina-Maria Guayacan-Carrillo, Siavash Ghabezloo, Jean Sulem, Darius M Seyedi, and Gilles Armand. Effect of anisotropy and hydro-mechanical couplings on pore pressure evolution during tunnel excavation in low-permeability ground. *International Journal of Rock Mechanics and Mining Sciences*, 97:1–14, 2017.

[27] L.-M. Guayacán-Carrillo, J. Sulem, D.M. Seyedi, S. Ghabezloo, A. Noiret, and G. Armand. Analysis of Long-Term Anisotropic Convergence in Drifts Excavated in Callovo-Oxfordian Claystone. *Rock Mechanics and Rock Engineering*, 49(1):97–114, 2016.

[28] M. Gutierrez, L.E. Øino, and R. Nygård. Stress-dependent permeability of a de-mineralised fracture in shale. *Marine and Petroleum Geology*, 17(8):895–907, 2000.

[29] D. Jougnot, A. Revil, N. Lu, and A. Wayllace. Transport properties of the Callovo-Oxfordian clay rock under partially saturated conditions. *Water Resources Research*, 46(8), 2010.

[30] M. Ki-Bok, J. Rutqvist, C.-F. Tsang, and L. Jing. Stress-dependent permeability of fractured rock masses: A numerical study. *International Journal of Rock Mechanics and Mining Sciences*, 41(7):1191–1210, 2004.

[31] O Kolditz. *Computational Methods in Environmental Fluid Mechanics*. Springer, Heidelberg, 2002. ISBN 978-3-662-04761-3.

[32] O. Kolditz, Th. Nagel, H. Shao, W. Wang, and S. Bauer. Thermo-Hydro-Mechanical-Chemical Processes in Fractured Porous Media: Modelling and Benchmarking - Benchmarking Initiatives. In *Terrestrial Environmental Sciences*, volume 3, page 260. Springer, Heidelberg, 2016. ISBN 978-3-319-29224-3.

[33] Olaf Kolditz, Sebastian Bauer, Lars Bilke, Norbert Böttcher, Jens Olaf Delfs, Thomas Fischer, Uwe-Jens Görke, Thomas Kalbacher, Georg Kosakowski, Christopher McDermott, Chan-Hee Park, Florin Radu, Karsten Rink, Haibing Shao, Hua Shao, Feng Sun, Yuanyuan Sun, Ashok Singh, Joshua Taron, Marc Walther, Wenqing Wang, Norihiro Watanabe, Y Wu, M Xie, and Björn Zehner. OpenGeoSys: An open source initiative for numerical simulation of thermo-hydro-mechanical/chemical (THM/C) processes in porous media. *Environmental Earth Sciences*, 67:589–599, 2012. doi: 10.1007/s12665-012-1546-x.

[34] J. Kozeny. Uber kapillare leitung der wasser in boden, sitzungsber. *Transactions of the Institution of Chemical Engineers*, 136:271–306, 1927.

[35] Roland W. Lewis and B. A. Schrefler. *The Finite Element Method in the Static and Dynamic Deformation and Consolidation of Porous Media*. Wiley, 1998. ISBN 978-0-471-92809-6.

[36] Y.-S. Ma, W.-Z. Chen, H.-D. Yu, Z. Gong, and X.-L. Li. Variation of the hydraulic conductivity of Boom Clay under various thermal-hydro-mechanical conditions. *Engineering Geology*, 212:35–43, 2016.

[37] Y.-S. Ma, W.-Z. Chen, Z. Gong, H.-D. Yu, F.-F. Li, and X.-L. Li. Coupled thermo-hydro-mechanical anisotropy characteristics of clay-Based on the ATLAS III in situ heating test. *Yantu Lixue/Rock and Soil Mechanics*, 39(2):426–436 and 444, 2018.

[38] M. Mahjoub, A. Rouabhi, M. Tijani, S. Granet, S. M'Jahad, and J. Talandier. Numerical study of Callovo-Oxfordian argillite expansion due to gas injection. *International Journal of Geomechanics*, 18(1), 2018.

[39] P. Marschall, S. Giger, R. De La Vassière, H. Shao, H. Leung, C. Nussbaum, T. Trick, B. Lanyon, R. Senger, A. Lisjak, and A. Alcolea. Hydro-mechanical evolution of the EDZ as transport path for radionuclides and gas: insights from the Mont Terri rock laboratory (Switzerland). *Swiss Journal of Geosciences*, 110(1):173–194, 2017.

[40] C.R. McKee, A.C. Bumb, and R.A. Koenig. Stress-dependent permeability and porosity of coal and other geologic formations. *SPE Formation Evaluation*, 3(1):81–91, 1988.

[41] H. Menaceur, P. Delage, A.M. Tang, and N. Conil. On the Thermo-Hydro-Mechanical Behaviour of a Sheared Callovo-Oxfordian Claystone Sample with Respect to the EDZ Behaviour. *Rock Mechanics and Rock Engineering*, 49(5):1875–1888, 2016.

[42] Anthony B Muller. *Geochemical Parameters Used in the Bedded Salt Reference Repository, Risk Assessment Methodology*. The Commission, 1981.

[43] B. Pardoen and F. Collin. Modelling the influence of strain localisation and viscosity on the behaviour of underground drifts drilled in claystone. *Computers and Geotechnics*, 85:351–367, 2017.

[44] B. Pardoen, S. Levasseur, and F. Collin. Using shear strain localisation to model the fracturing around gallery in unsaturated Callovo-Oxfordian claystone. *Springer Series in Geomechanics and Geoengineering*, none:285–291, 2015.

[45] B. Pardoen, J. Talandier, and F. Collin. Permeability evolution and water transfer in the excavation damaged zone of a ventilated gallery. *International Journal of Rock Mechanics and Mining Sciences*, 85:192–208, 2016.

[46] C. Plúa1, M.N. Vu, G. Armand, J. Rutqvist, J. Birkholzer, H. Xu, R. Guo, K.E. Thatcher, A.E. Bond, W. Wang, T. Nagel, H. Shao, and O. Kolditz. A reliable numerical analysis for large-scale modelling of a high-level radioactive waste repository in the callovo-oxfordian claystone. *International Journal of Rock Mechanics and Mining Sciences*, under review, 2020.

[47] T. Popp, K. Salzer, and W. Minkley. Influence of bedding planes to edz-evolution and the coupled hm properties of opalinus clay. *Physics and Chemistry of the Earth*, 33(SUPPL. 1):S374–S387, 2008.

[48] Allen M Rowe Jr and James CS Chou. Pressure-volume-temperature-concentration relation of aqueous sodium chloride solutions. *Journal of Chemical and Engineering Data*, 15(1):61–66, 1970.

[49] D. Seyedi, C. Plua, C. Vitel, G. Armand, J. Rutqvist, J.T. Birkholzer, N.N. Xu, N.N. Guo, K. Thatcher, A. Bond, W.Q. Wang, Th. Nagel, H. Shao, and O. Kolditz. A numerical benchmark exercise for thermo-hydro-mechanical modeling of an in situ heating test in the Callovo-Oxfordian claystone. *International Journal of Rock Mechanics and Mining Sciences*, 2019. submitted.

[50] Darius Seyedi. Specifications for DECOVALEX 2019 Task E : multi-scales heater experiments upscaling of modelling results from small scale to one to one scale. 2016.

[51] D.M. Seyedi, C. Plúa1, M.N. Vu, G. Armand, J. Rutqvist, J. Birkholzer, H. Xu, R. Guo, K.E. Thatcher, A.E. Bond, W. Wang, T. Nagel, H. Shao, and O. Kolditz. Upscaling THM modelling from small-scale to full-scale in-situ experiments in the Callovo-Oxfordian claystone. *International Journal of Rock Mechanics and Mining Sciences*, under review, 2020.

[52] O. Stephansson, J. Hudson, and L. Jing. *Coupled Thermo-Hydro-Mechanical-Chemical Processes in Geo-Systems Fundamentals, Modelling, Experiments and Applications*, volume 2. Elsevier Geo-Engineering Book Series, 2004. ISBN 978-0-08-044525-0.

[53] C.F. Tsang, J.D. Barnichon, J. Birkholzer, X.L. Li, H.H. Liu, and X. Sillen. Coupled thermo-hydro-mechanical processes in the near field of a high-level radioactive waste repository in clay formations. *International Journal of Rock Mechanics and Mining Sciences*, 49:31–44, 2012.

[54] R. Walsh, C. McDermott, and O. Kolditz. Numerical modeling of stress-permeability coupling in rough fractures. *Hydrogeology Journal*, 16 (4):613–627, 2008. doi: 10.1007/s10040-007-0254-1.

[55] W. Wang and et al. Program development and investigation of coupled thermal, hydraulic, mechanical and chemical (THMC) processes (Programmentwicklung und Untersuchung von gekoppelten thermischen, hydraulischen, mechanischen und chemischen (THMC) Prozessen). Technical Report 2, Helmholtz-Zentrum für Umweltforschung GmbH - UFZ, UFZ Leipzig, Permoserstr. 15, 2019.

[56] W.J. Xu, H. Shao, J. Hesser, W. Wang, K. Schuster, and O. Kolditz. Coupled multiphase flow and elasto-plastic modelling of in-situ gas injection experiments in saturated claystone (mont terri rock laboratory). *Engineering Geology*, 157:55–68, 2013.

[57] C.-L. Zhang. The stress-strain-permeability behaviour of clay rock during damage and recompaction. *Journal of Rock Mechanics and Geotechnical Engineering*, 8(1):16–26, 2016.

[58] Chun-Liang Zhang. Sealing of fractures in claystone. *Journal of Rock Mechanics and Geotechnical Engineering*, 5(3):214–220, jun 2013. ISSN 16747755. doi: 10.1016/j.jrmge.2013.04.001. URL http://dx.doi.org/10.1016/j.jrmge.2013.04.001https://linkinghub.elsevier.com/retrieve/pii/S1674775513000334.

[59] R.W. Zimmerman. Thermal conductivity of fluid-saturated rocks. *Journal of Petroleum Science and Engineering*, 3(3):219–227, 1989. doi: 10.1016/0920-4105(89)90019-3. URL https://www.scopus.com/inward/record.uri?eid=2-s2.0-0024857393&doi=10.1016%2f0920-4105%2889%2990019-3&partnerID=40&md5=e94c9da02d78ea4e74038b9366bc17e6.

Acronyms (alphabetically)

ANDRA	French national radioactive waste management agency (https://international.andra.fr/)
ALC	Full-scale heater experiment at MHM
COx	Callovo-Oxfordian clay rock
DECOVALEX	DEvelopment of COupled models and their VALidation against EXperiments
EDZ	Excavation-Damaged Zone
EOS	Equation of state
GED	A drift in the MHM URL
HE-D, HE-E	In-situ heater experiments in the Mont Terri URL
HM	Hydro-Mechanical
IAWPS	International Association for the Properties of Water and Steam (www.iapws.org)
IF97	Water density formula developed by IAWPS
M/HM	Meuse/Haute-Marne (https://international.andra.fr/sites/international/files/2019-03/CMHM_2015_Version2017_EN_relu_planche_1.pdf)
OGS	OpenGeoSys
OPA	Opalinus clay
REV	Representative elementary volume
TED	Small-scale heater experiment at MHM
TEDnumber	Sensor positions of the TED experiment
THM	Thermo-Hydro-Mechanical
URL	Underground Research Laboratory